Improved Well Index Calculation for Accurate Modeling of Well Position in Heterogeneous Reservoirs

Master Thesis

Annique Godschalk

Delft University of Technology

TU Delft

Improved Well Index Calculation for Accurate Modeling of Well Position in Heterogeneous Reservoirs

by

Annique Godschalk

to obtain the degree of Master of Science

at the Delft University of Technology,

to be defended publicly on Thursday July 17, 2025 at 16:00 PM.

Student number:	5244455	
Project duration:	February 10, 2025 – June 18, 2025	
Thesis committee:	Dr. D.V. Voskov,	TU Delft, chair
	Dr. P. Rulff,	TU Delft, committee member
	Dr. A. Daniilidis,	TU Delft, committee member

An electronic version of this thesis is available at `http://repository.tudelft.nl/`.

TU Delft

Abstract

The presence of wells in reservoir simulations can be represented by utilizing a well model within the finite volume framework of the simulator. A commonly applied approach is the Peaceman well inflow model, which places wells at the center of a specified grid cell of the reservoir model. Nonetheless, several studies have investigated the ability of placing wells *off-center*. Capturing the exact well position can significantly impact the reservoir response of the simulation model, particularly for heterogeneous reservoirs, as spatial heterogeneity plays a more pronounced role when wells are no longer located at the center of the grid cell. Furthermore, exact well position modeling would allow for more realistic well presentation within the reservoir simulator. Although the performed studies have successfully modeled wells *off-center*, they are course-grid approaches. Therefore, this study investigates the application of an unstructured grid-based well model to accurately account for both the exact well location within a grid block and the surrounding reservoir heterogeneity in the calculation of a steady-state well index.

To achieve this, an improved well inflow model is established using Gmsh (three-dimensional finite element mesh generator) and the open Delft Advanced Research Terra Simulator (open-DARTS). The model implements an unstructured grid on a locally structured reservoir geometry, where typically five structured blocks are integrated. The model is verified against the Peaceman well inflow model for a center position and values match the Peaceman well model with a 5% accuracy. The model is validated for different well placements, permeability profiles and a considered number of structured reservoir blocks. Additionally, the validation study includes an accuracy assessment of the model against a full unstructured approach. The improved well index model is finally applied to the wells of the Geothermie Delft (GTD) project, enabling well index estimations based on true well trajectories.

Validation of the model shows that both well placement and local reservoir permeability impact the computed well index. A comparison of the proposed well index evaluation with the fully unstructured model indicates that incorporating more surrounding reservoir blocks within the well index calculation leads to closer correspondence with the fully unstructured approach. Additionally, the study reveals that the spatial discretization method within the finite volume framework used in open-DARTS influences well index values and can result in errors, depending on the choice of discretization approach. Finally, the results of the application of the proposed approach to the real trajectory of wells in the Geothermie TU Delft (GTD) project demonstrate that the improved well index model generally yields lower well index estimations than the Peaceman well model. The effect of this difference is further tested by simulating the full reservoir with the newly obtained well index values. These results depict that the well pressure profile for both the injector and producer varies depending on the well model, especially for later simulation times. The improved well model captures more variations in the pressure profile, emphasizing its capability for more accurate well modeling.

Acknowledgments

Firtstly, I would like to thank my supervisor, Dr. Denis Voskov, for the opportunity and support during this project. The weekly meetings helped me tremendously in shaping the research correctly and obtaining the desired outcomes. Furthermore, the opportunity to work and extend my knowledge in reservoir simulation and the open-DARTS simulator will remain to hold great value to me. This holds particular meaning as I have always found reservoir simulation fascinating, despite having limited exposure to it prior to my master's.

Additionally, I am grateful of Ilshat Saifullin and the rest of the open-DARTS development team for the constant help and willingness to assist with my questions regarding the simulator or any other encountered implications. I always felt welcomed and encouraged, and their help and time significantly contributed to the progress of my project. I am especially grateful to Yuan Chen for conducting the full reservoir simulations. Their effort was instrumental in completing the final stages of the research and is sincerely appreciated.

I would like to give a special thank you to my committee members Paula Rulff and Dr. Alexandros Daniilidis. They have provided me with valuable feedback and new insights on the project, that I would not have come up with by myself. They helped me improve the project and gave valuable additions in how to communicate the message of the study effectively.

I wish to mention my gratitude to my close family and friends for the aid they have given me throughout the entire process. From coffee breaks to dinners and walks, your presence is immensely appreciated.

Lastly, I would like to dedicate this work to my mother, Ilse, whose love, encouragement, and support were a constant source of inspiration. Her support during the project ranged from helping me focus on the correct tasks to mentally support me by reminding me how proud she was of my achievements. Therefore, her belief in me gave me a great amount of strength throughout this thesis project. Though she is no longer with me and my family, her presence in my mind and heart still influence the choices I make and the person I strive to become. Thank you for everything you have taught me.

Annique Godschalk
Delft, July 2025

Contents

1

Introduction

To transition from fossil fuels to renewable forms of energy and to reduce the carbon footprint, geothermal energy has become an increasingly relevant source of energy and currently holds the fourth spot for renewable energy in the Netherlands [9, 30]. To quantify the growth of geothermal energy in the Netherlands, the produced heat over the past 17 years is illustrated in Figure 1.1 [16]. To meet the demand for net-zero emissions by 2050, renewable energy production needs to grow, and geothermal energy can play a key role in this task, to decrease dependency on hydrocarbons in the form of heating houses and surrounding buildings with warm water produced from the deep subsurface. In 2023, the cumulative annual energy produced by geothermal energy sources was 6.875 PJ in the Netherlands. Nonetheless, the growth of this energy sector has stagnated in the last four years and is currently mostly used for the heating of greenhouses [9]. Geothermal energy has the potential to provide for 25% of the heat demand of the built environment of the Netherlands [19]. Hence, for it to play a significant role in the energy transition, the geothermal energy sector must expand further and increase the number of projects supplying heat to the built environment.

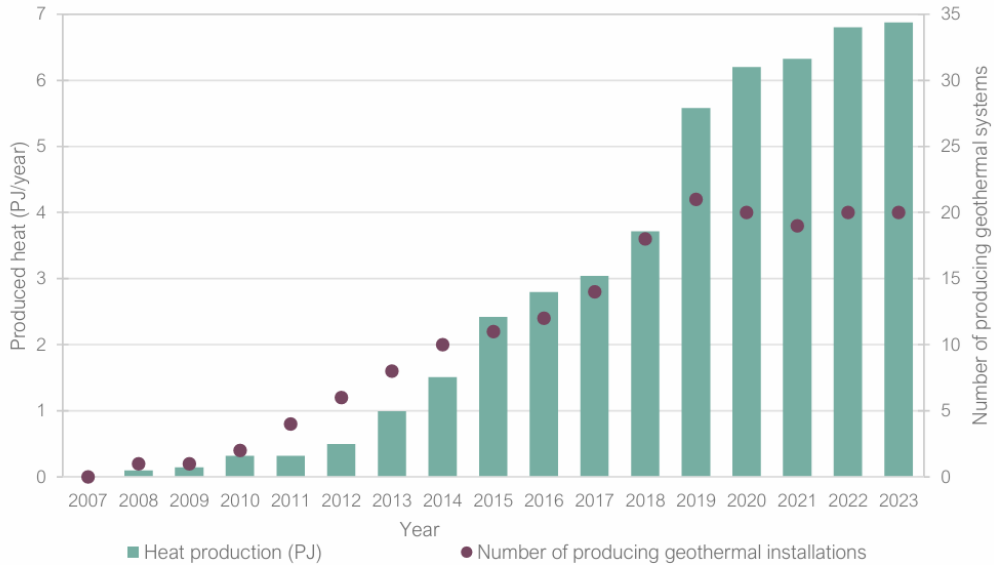

Figure 1.1: The growth of geothermal energy in the Netherlands from 2007 to 2023 [16].

Feasibility and viability analyses of geothermal projects directly impact the realization of such projects. For such an analysis, well placement is a key reservoir management decision that highly influences the net present value (NPV), a financial metric to asses economic project viability, and reservoir response, which describes the behavior of temperature and pressure of the geothermal system over time [11]. Therefore a well-placed strategy plays a significant role in the decision on project evaluation. To perform

project feasibility analyses and determine the correct well placement strategy, reservoir simulation is an important tool to predict reservoir performance and fluid flow in various conditions [3]. Within numerical reservoir simulation the finite volume method plays an important role in the spatial discretization of the energy and mass conservation equations [13]. A simulator, used in this study, that employs the finite volume method is known as the open Delft Advanced Research Terra Simulator (open-DARTS) [29]. Before incorporating wells into the reservoir model and evaluating the reservoir response, the desired scale of reservoir representation needs to be determined. Based on this scale and corresponding heterogeneity representation, spatial discretization is applied, and the well model can subsequently be integrated within the finite volume framework of the simulator.

A well model is added to account for the presence of wells within the reservoir. Wells are typically selected manually and placed in the center of a designated grid cell. They are then evaluated using the Peaceman well inflow model, employing a well index calculation [21]. This well index relates bottom hole well pressure to the pressure of the well block, and is based on the assumption of single-phase incompressible steady-state radial flow [32]. However, for reservoirs containing a high degree of heterogeneity, placing wells at different locations (*off-center*) within the original grid block can crucially impact the response of the simulation model and ultimately affect the net present value. Additionally, modeling wells *off-center* allows for more realistic well position modeling, impacting reservoir response and fluid flow behavior of the simulation model. In this regard, accurate well modeling is key in assessing the viability and feasibility of a project.

Several research papers have examined strategies for placing wells at an exact position within the designated well block. Peaceman [22] stated that the numerical equivalent radius for an isolated well, where the equivalent radius is defined as the point where the pressure of the radial flow matches that of the grid block, does not depend on its position inside the well block [21]. Nevertheless, it was found that for wells in non-center positions, the fluid flow in the vicinity of the well was not represented correctly [6, 26]. Hence, although the equivalent radius stays constant, the correct fluid flow pattern is not honored when evaluating the finite-difference equations for exact well placements.

Subsequently, multiple *off-center* methods have been established, accounting for the correct fluid flow pattern, examples of such are the methods proposed by Su [26] and Ding, Renard, and Weill [6]. The method suggested by Su [26] introduces a new well equation, which causes more reservoir terms to have a well term in their approximation. Although the method has shown promising results, it is complicated, and its implementation is not straightforward. Ding, Renard, and Weill [6] put forward a simpler method by establishing equivalent transmissibilities such that the conventional well index formula, as described by Peaceman [21], can still be applied. In other words, transmissibility values are modified to account for the correct fluid-flow behavior. Notwithstanding that both methods have lead to improved results, both approaches make use of a coarse-grid approach. An alternative method to model exact well positions is by incorporating unstructured grid refinement [26].

Therefore, this research will investigate the application of an unstructured grid within the well-inflow model for reservoir simulation. The thesis aims to improve well index calculations to be able to account for an exact well position and surrounding reservoir heterogeneity. This will be performed by means of unstructured grid refinement and calculation of a local well index based on simulation results obtained with the open Delft Advanced Research Terra Simulator (open-DARTS).

1.1. Problem statement

The research goal, as described, can be captured by answering the following main and sub-research questions.

Main research question

"How can one account for an exact position of the well within the grid block and heterogeneity of the reservoir in the calculation of a steady-state well index using an unstructured grid approach?"

Sub-research questions

(I). How does the local well index result using an unstructured mesh compare in terms of accuracy against a fully unstructured approach or analytic solution?

(II). How will the influence of reservoir heterogeneity be covered by the proposed approach?

(III). What is the effect of the different spatial discretization techniques within the finite volume framework of the simulator on the well index model?

(IV). How does the proposed method affect well index calculation along a real well trajectory?

To answer the main and sub-research questions, an improved well index calculation method is established within open-DARTS. The geometry of this model closely follows the geometrical model that was introduced by Peaceman [21]. Verification of the model is performed by comparison with the results of the Peaceman approach. Secondly, model validation is carried out for different scenarios, including a two-dimensional synthetic reservoir. Finally, the established model will be tested for the wells of the Geothermie Delft project (GTD). The model aims to obtain well index values for the reservoir based on the true well trajectory of the doublet. The impact of the improved well index model on the simulation reservoir response of the GTD reservoir model is tested by comparison of the full simulation results with the Peaceman well index model.

Ultimately, both a two-point flux approximation (TPFA) and a multipoint flux approximation (MPFA) are examined as discretization methods within the finite volume framework of open-DARTS. The study will evaluate the variations introduced by each discretization approach.

1.2. Thesis structure

The following thesis structure is pursued:

- Chapter 1: Introduction and research questions
- Chapter 2: Theoretical framework
- Chapter 3: Introduction to improved well index model
- Chapter 4: Systematic validation study
- Chapter 5: Application to GTD reservoir
- Chapter 6: Discussion
- Chapter 7: Conclusion

2

Theoretical framework

This chapter will discuss all relevant background theory needed to understand the finite volume method and well model within reservoir simulation more thoroughly. Within chapter 1, reservoir simulation and the role of the finite volume method within the simulator were introduced. Open-DARTS allows for a two-point flux approximation (TPFA) and a multipoint flux approximation (MPFA) in the finite volume framework. Therefore, these two discretization methods will be explained further. Secondly, the simulator's well model is presented through a discussion of various fluid flow regimes.

2.1. Numerical discretization techniques

Within the finite volume scheme, two discretization techniques can be employed for approximating the fluid flow equations within the open-DARTS simulator, namely the TPFA and MPFA approximations. This section will introduce both techniques using an example of incompressible single-phase flow without gravity [23] [8]. In Equation 2.1 and Equation 2.2, the mass conservation equation and Darcy's law are presented and these serve as the governing equations for the finite volume method within the simulator [24]. Within these formulas, $\mathbf{u}$ is the flux, $\mathbf{K}$ the permeability tensor, μ is the viscosity and the pressure is defined by P:

$$\nabla \cdot \mathbf{u} = q, \tag{2.1}$$

$$\mathbf{u} = -\frac{\mathbf{K}}{\mu} \nabla P. \tag{2.2}$$

2.1.1. Two-point flux approximation

The two-point flux approximation (TPFA) follows the finite volume discretization method and uses two points to estimate the flux across an interface between two neighboring cells. Figure 2.1 shows the TPFA scheme geometry that is generally followed [8]. Within the figure the neighboring cells are expressed by E_i and E_j, the interface separating these cells is written as e. Furthermore, centroids and the cell pressures are denoted by x and P_E, respectively. Lastly, two vectors are identified, namely; $\mathbf{r}^e_{E_i}$ and $\mathbf{n}^e_{E_i}$. $\mathbf{r}^e_{E_i}$ stands for the vector starting in x_{E_i} and going to the face centroid x_e, and $\mathbf{n}^e_{E_i}$ the unit normal vector on face e out of the cell.

To find the discretization following the TPFA scheme as presented above, Equation 2.1 is written in integral form over a single cell E_i

$$\int_{E_i} \nabla \cdot \mathbf{u} \; dV = \int_{E_i} q \; dV. \tag{2.3}$$

The left-hand side of this equation is evaluated using integration by parts; this results in the expression as presented by Equation 2.4

$$\int_{E_i} \nabla \cdot \mathbf{u} \; dV = \sum_{e \in \partial E_i} \int_e \mathbf{u} \cdot \mathbf{n}^e_{E_i} \; dS. \tag{2.4}$$

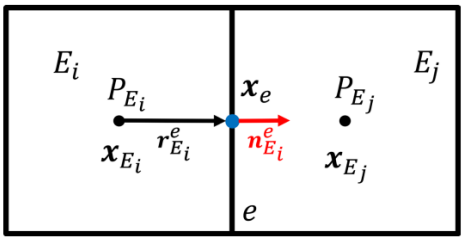

Figure 2.1: Figure of the two-point flux approximation scheme that is used for the spatial discretization [8].

Finally, the numerical flux of surface e can be evaluated using the TPFA scheme and the above equation. This results in the expression presented in Equation 2.5. Within this formula, $T_{i,j}$ and $T_{j,i}$ represent the half transmissibility calculated from the side of cell E_i and E_j, respectively. T_{ij} is the transmissibility between E_i and E_j. The half transmissibilities can be calculated according to Equation 2.6 and Equation 2.7:

$$\int_e \mathbf{u} \cdot \mathbf{n}^e_{E_i} dS \approx (T^{-1}_{i,j} + T^{-1}_{j,i})^{-1}(P_{E_i} - P_{E_j}) = T_{ij}(P_{E_i} - P_{E_j}), \tag{2.5}$$

$$T_{i,j} = |e| \frac{\mathbf{K}_{E_i} \mathbf{r}^e_{E_i}}{\mu_{E_i} |\mathbf{r}^e_{E_i}|^2} \cdot \mathbf{n}^e_{E_i}, \tag{2.6}$$

$$T_{j,i} = |e| \frac{\mathbf{K}_{E_j} \mathbf{r}^e_{E_j}}{\mu_{E_j} |\mathbf{r}^e_{E_j}|^2} \cdot \mathbf{n}^e_{E_j}. \tag{2.7}$$

Within the above formula's $|e|$ is the area of the interface e and $|\mathbf{r}^e_E|$ is the length of the vector $\mathbf{r}^e_E$. The TPFA method can result in errors when a mesh is not K-orthogonal. For a grid to be K-orthogonal, the vector $\mathbf{K}_E \mathbf{n}^e_E$ needs to be parallel to the vector $\mathbf{r}^e_E$. This K-orthogonality can not always be guaranteed for unstructured grids, thus possibly leading to negative transmissibilities and numerical errors.

2.1.2. Multipoint flux approximation

The multipoint flux approximation (MPFA) method is established to overcome the TPFA defects for non-K-orthogonal grids [15]. Multiple types of MPFA discretization methods have been formulated and are reported by Aavatsmark [1]. Generally, these methods follow the assumption that the flux across interface e can be written as Equation 2.8, assuming incompressible single-phase flow without gravity [15]

$$F_e = \sum_{j \in J} T_{ij} P_j. \tag{2.8}$$

In Equation 2.8, the set J represents six cells that are a subset of the full grid. An example of such a set is shown in Figure 2.2, and the cell set surrounds the interface e.

To calculate the transmissibility T_{ij} from Equation 2.8, the pressure is evaluated at the center of each grid cell, and a dual grid is created connecting the cell midpoint to the interface midpoints [1]. This dual grid is illustrated by Figure 2.3, additionally, the dual grid is extended outside of the primary grid. A cell of the dual grid is also referred to as an interaction region. This region will estimate the transmissibility coefficients for each subinterface. The dual grid splits the cell interfaces in a total of four subinterfaces for three-dimensional problems and two subinterfaces for two-dimensional grids. Finally, the transmissibility coefficients for the cell interfaces are calculated by combining the transmissibility values of the subinterfaces.

Determining the subinterface transmissibility follows a piecewise linear variation of the pressure on each cell present in the interaction region [15]. Accordingly, continuity conditions of pressure and flux are applied to estimate the transmissibility coefficients. Different existing methods use varying conditions and points of continuity, one of the most prominent methods is the MPFA-O method. This method introduces continuity of the flux across subinterfaces and continuity of the pressure at the interface midpoints. The inactive or outside cells are dealt with by defining the permeability tensor to be equal to zero [1].

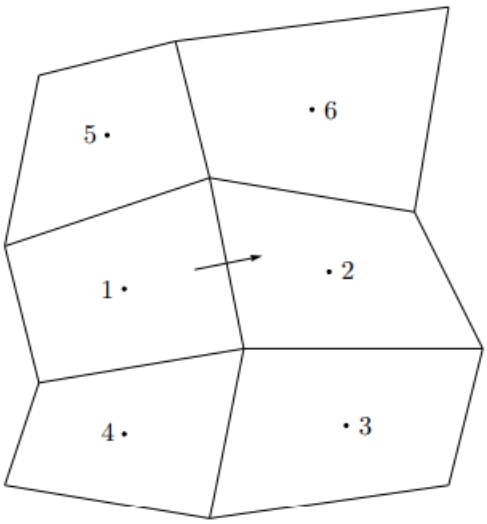

Figure 2.2: The geometric scheme for the multipoint flux approximation method in 2D [15].

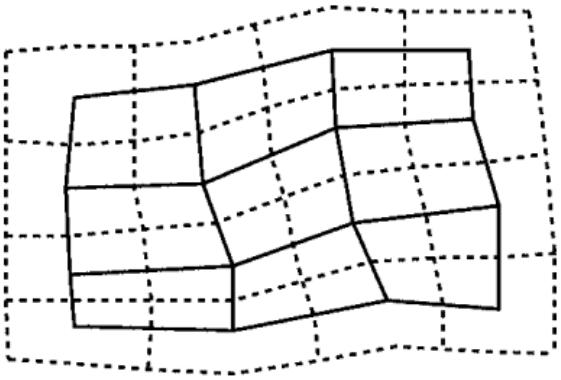

Figure 2.3: The primary grid and the dual grid are drawn over the primary grid using dashed lines [1].

Finally, it should be noted that in situations involving high anisotropy ratios combined with significant variations in heterogeneity, the MPFA-O method might produce unexpected signs in transmissibility coefficients [1]. This can result in the transmissibility coefficients turning negative, and the solution can consequently behave non-monotonic, thus causing under- or over-estimations for the pressure solution [18].

2.2. Flow regimes and Well modeling

In this section, we briefly describe different flow regimes and the conventional modeling approach for wells in reservoir simulation.

2.2.1. Flow Regimes

To be able to characterize fluid flow behavior and reservoir pressure response over time, a total of three flow regimes need to be identified [2] [5]. These regimes are steady-state flow, semi-steady-state flow and transient flow.

Steady-state flow holds when the pressure (p) at any location i in the reservoir is constant over time (t). The mathematical formulation of this is presented below by Equation 2.9.

$$\left(\frac{\partial p}{\partial t}\right)_i = 0. \tag{2.9}$$

In other words, the underlying assumption is that the fluid withdrawal from a cell will exactly equal the fluid inflow, assuming open-boundary flow for the cell. The steady-state condition is further applicable when pressure is supported in the reservoir by either natural water influx or fluid injection.

The semi-steady-state condition applies to a reservoir that has been producing for an adequate period; thus, the influence of the outer reservoir boundaries has been experienced. This outer boundary is felt as a ”brick wall”; therefore, there is no flow of fluids into the radial cell with radius r_e [5]. At this boundary, the following expression holds;

$$\frac{\partial p}{\partial r} = 0. \tag{2.10}$$

Finally, when a well produces at a constant rate, the reservoir pressure at every position and time for the semi-steady-state can be described by Equation 2.11.

$$\left(\frac{\partial p}{\partial t}\right)_i = \text{constant}. \tag{2.11}$$

Transient flow is described as a short period of time, where pressure and the pressure derivative with respect to time are not zero or constant. This condition is related to the short period after a pressure disturbance has been initiated in the reservoir; in this period, the reservoir will behave as infinite. The mathematical expressions representing transient flow are presented in Equation 2.13. Both pressure and pressure derivative are described by functions g and f that are dependent on location (i) and time (t).

$$p = g(i,t) \tag{2.12}$$

$$\text{and,} \quad \left(\frac{\partial p}{\partial t}\right) = f(i,t). \tag{2.13}$$

The flow regimes and their respective schematic pressure derivatives over time are shown in Figure 2.4 below. Figure 2.4 shows that for steady-state flow pressure stays constant over time and thus no decline in pressure is observed. Semi-steady-state flow decreases linearly and its derivative is described by a constant factor. Lastly, for transient flow, the pressure decreases according to the function f over time, which is dependent on the location within the reservoir and time.

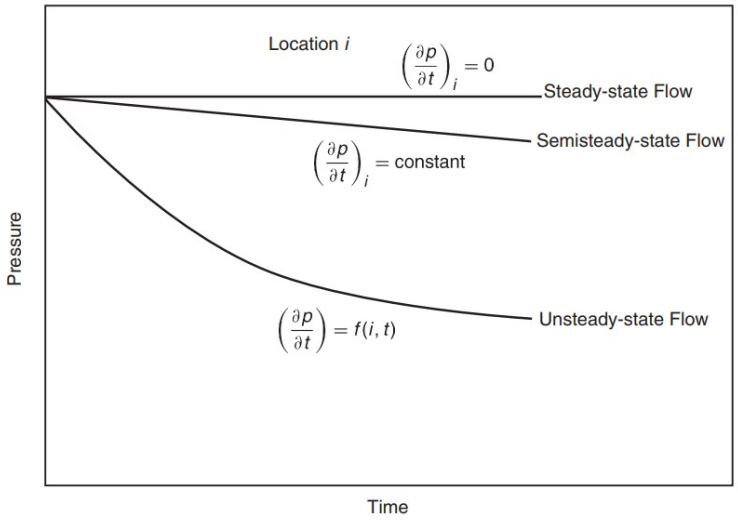

Figure 2.4: Schematic pressure decline of the three defined flow regimes; steady state, semi-steady state and transient flow [2].

2.2.2. Steady-state flow: Peaceman's Model

The theoretical framework of this study includes the Peaceman well inflow model that is typically set as the well model within reservoir simulation [21]. This approximation correlates the bottom hole pressure

of the well to that of the pressure of the reservoir block containing the well by assuming single-phase incompressible steady-state radial flow. Furthermore, the method assumes a vertical well in a uniform Cartesian grid, fully penetrating the grid block [25]. The pressure distribution around a radial source for single-phase flow is;

$$p(r) = p^w + \frac{q^w \mu}{2\pi k h} \cdot \ln\left(\frac{r}{r_w}\right). \tag{2.14}$$

Here μ is the viscosity, k the permeability, h the thickness, r the radial distance from the well and q_w and r_w the well inflow and radius, respectively. Following Equation 2.14 the pressure for the well block (block zero: p_0 or $p^{i,j}$) can be defined similarly, as;

$$p_0 = p^w + \frac{q^w \mu}{2\pi k h} \cdot \ln\left(\frac{r_0}{r_w}\right). \tag{2.15}$$

From Equation 2.15, r_0 is defined as the radius where the pressure of the radial flow equation is equal to the block pressure p_0. This also follows from Figure 2.5. Figure 2.5 shows a 5-block reservoir geometry with the center block containing a well in its center.

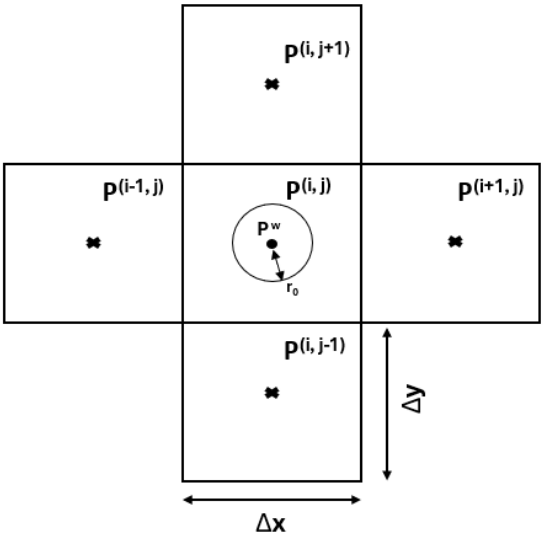

Figure 2.5: 5-block reservoir geometry, the center block contains a well at its center. The Peaceman radius is presented by r_0, corresponding to the radius at which pressure from radial flow equals the block pressure.

For the reservoir blocks neighboring the well block, the pressure can likewise be described by Equation 2.14, which results in Equation 2.16. Here, a is equal to Δx and Δy for square grid blocks, which indicates the distance from the well to the center of the neighboring block

$$p_i = p_0 + \frac{q^w \mu}{2\pi k h} \cdot \ln\left(\frac{a}{r_0}\right). \tag{2.16}$$

Equation 2.16 is combined with the assumption that the well inflow for the case presented in Figure 2.5 should equal the inflow of each of the four surrounding blocks. Using Darcy's assumptions for steady-

state flow the well inflow term is derived accordingly [7].

$$q^w = \sum_{i=1}^{4} q_i \tag{2.17}$$

$$q_i = \frac{kA}{\mu}\frac{p_i - p_0}{a}, \text{ using } A = ha \tag{2.18}$$

$$q^w = \frac{kh}{\mu}\left(\sum_{i=1}^{4} p_i - 4p_0\right). \tag{2.19}$$

Combining Equation 2.19 and Equation 2.16 Peaceman [21] found that $r_0/a \approx 0.208$. This relationship defines the well index (WI) for square grid blocks accordingly to Equation 2.20

$$\mathsf{WI} = \frac{2\pi kh}{\ln\frac{r_0}{r_w}}, \text{ with } r_0 = 0.208a. \tag{2.20}$$

This well index is used in reservoir simulation to relate well pressure to that of the well block [6], and can finally be written as

$$q^w = \frac{\mathsf{WI}}{\mu}(p_0 - p^w). \tag{2.21}$$

Well inflow model in open-DARTS

The well inflow model that is implemented in the open-DARTS is the Peaceman well inflow model altered for non-square grid blocks and anisotropic permeability [25] [20]. The well index is then defined as;

$$\mathsf{WI} = \frac{2\pi\sqrt{k_x k_y}\Delta z}{\ln\left(\frac{r_0}{r_w}\right) + s}, \tag{2.22}$$

where s is the skin factor. The skin factor is a measure of deviation from perfect radial inflow because of different types of damage (e.g., invasion of drilling fluid) or enhancement (e.g., hydraulic fracturing), reservoir perforation shape, depth, angle, the crushed zone, or possible combinations of the above factors [33]. Within Equation 2.22 Δz is the reservoir thickness, and hence represents the same as h in previous formulas.

The radius r_0 in Equation 2.22 is defined as:

$$r_0 = \frac{\left(\left(\frac{k_y}{k_x}\right)^{\frac{1}{2}}\Delta x^2 + \left(\frac{k_x}{k_y}\right)^{\frac{1}{2}}\Delta y^2\right)^{\frac{1}{2}}}{\left(\frac{k_y}{k_x}\right)^{\frac{1}{4}} + \left(\frac{k_x}{k_y}\right)^{\frac{1}{4}}}. \tag{2.23}$$

Lastly, the well index is multiplied by Darcy's constant c, where c = 0.008526. Which translates the well index to metric units. Thus with;

- Length in meters,
- Time in days,
- Permeability in mDarcy,
- Pressure in Bars,
- Mass in moles,
- Viscosity in cPoise.

2.2.3. Other flow regimes

Semi-steady-state solution

The constant as defined in Equation 2.11 can be derived and is used to find the general analytical relationship between pressure and radius r for the semi-steady-state condition [5]. The semi-steady-state constant is defined in Equation 2.24, and the obtained general relationship between p and r is presented by Equation 2.25

$$\frac{\partial p}{\partial t} = -\frac{q}{c\pi r_e^2 h\phi}, \tag{2.24}$$

$$p - p^w = \frac{q\mu}{2\pi kh}\left(\ln\frac{r}{r_w} - \frac{r^2}{2r_e^2}\right). \tag{2.25}$$

Within Equation 2.24 and Equation 2.25 ϕ is reservoir porosity, r_e is the drainage radius of the reservoir [27]. Furthermore, the inflow equation for semi-steady-state can also be expressed with respect to the average radial cell pressure. This follows the derivation by Dake [5] and results in the specified relation:

$$\bar{p} - p^w = \frac{q\mu}{2\pi kh}\left(\ln\frac{r_e}{r_w} - \frac{3}{4}\right). \tag{2.26}$$

Transient solution

The transient condition is often used to perform analysis on well tests; therefore, these analyses often make use of constant flow rate wells [2]. The solution for the radial diffusivity equation for transient flow is then also referred to as the constant terminal rate solution and can be approximated by a line source solution. For the time the transient solution holds, the pressure of the well bore can be related to the initial pressure (p_i) according to Equation 2.27 [5]

$$p^w = p_i - \frac{q\mu}{4\pi kh}\left(\ln\frac{4kt}{\gamma\phi\mu\beta r_w^2}\right). \tag{2.27}$$

Within Equation 2.27 q is defined as the flow rate, γ refers to Euler's constant, and β is the compressibility, including both the contribution of formation and fluid compressibility [4].

3

Improved well index model

The improved well index model will employ a so-called '5-block' unstructured grid that uses the two-dimensional geometrical scheme of a structured reservoir consisting of five square blocks, matching the geometric scheme in Figure 2.5 for the Peaceman well model closely. The creation of the model's unstructured mesh is executed using Gmsh, a software designed for finite-element mesh generation. The meshing strategy followed within Gmsh and the well index determination using the implementation of an unstructured grid within open-DARTS are further elaborated within the following sections.

3.1. Meshing Strategy

To model unstructured grids within open-DARTS, the software Gmsh is utilized to generate meshes. Gmsh is used as the Python package version, rather than building the meshes within the interface of Gmsh. As mentioned, a '5-block' structured case following the geometry in Figure 2.5, consisting of five square grid blocks, is used as the geometrical scheme, and will thus serve as the background grid.

The unstructured mesh is built around this structured geometric scheme, inspired by the strategy proposed in Li et al. [17]. The dimensions for a single structured grid block in the model are: Δx = 100 m and Δy = 100 m. To model the well, a cylindrical geometry is added within the mesh. The radius of this geometrical object equals r_{well}; furthermore, the wellbore is an empty geometry residing inside the mesh. Surrounding this well, another radial geometry is added with radius r_{well} + 0.1 m. This is done to ensure consistent shapes for the unstructured grid in the proximity of the well; therefore, a coherent well model is established within open-DARTS, and this ultimately enables reliable well index determination. This will be especially evident for the systematic model validation. The following parameters were further defined for the mesh.

- r_{well} is 0.152 m.
- Reservoir thickness h is 10 m. The mesh is thus extruded over 10 meters.
- Grid resolution at the well is 0.1 m (cl1).
- Grid resolution at the boundaries of the background grid is 5 m (cl2).
- Grid resolution at the additional radial geometry is 0.1 (cl3).

Finally, the resulting unstructured mesh corresponding to a structured 5-block geometry is obtained and presented within Figure 3.1. Additionally, a close-up showing the well geometry and the supplementary radial geometry is likewise presented. The presented mesh contains a well placed in the center, x = 150 m and y = 150 m, of the structured block. By using a smaller grid resolution at the well than at the boundaries of the structured grid blocks, there is mesh refinement towards the well. Lastly, before exporting the mesh, boundary faces, top, bottom, well and side faces, and matrix cells are assigned and labeled within the mesh, ensuring the mesh can be accurately read by the simulator.

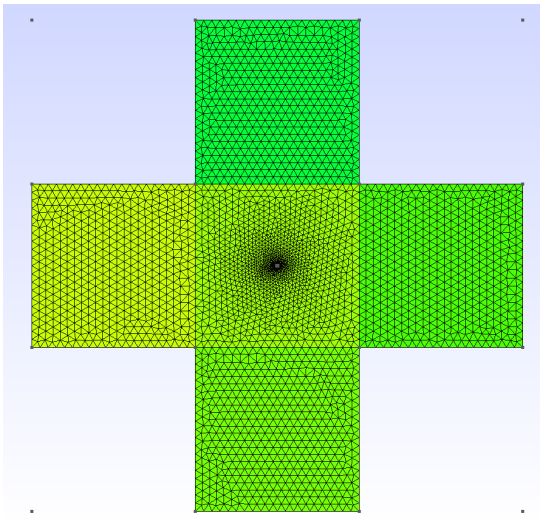

(a) The generated mesh, with the structured case containing five square grid blocks and the higher-resolution unstructured grid inside. Every structured grid block has dimensions of 100 by 100 meters.

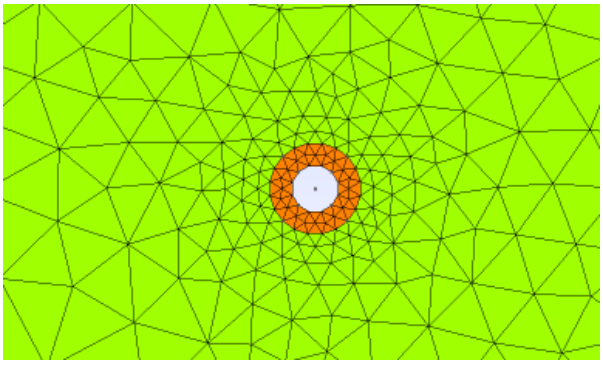

(b) Cylindrical geometry representing the well and the added radial geometry to ensure a consistent unstructured grid in the close proximity of the well. Domain size of this figure is approximately 3 meters in the x-direction and 2.5 meters in the y-direction.

Figure 3.1: The generated mesh using Gmsh, the well geometry is located at the center of the center structured block.

3.2. Well Index Calculations

The resulting unstructured mesh is read by open-DARTS, and discretization of the mesh is performed by the simulator, using a two-point flux approximation (TPFA). The two-point flux approximation was chosen due to simplicity and robustness. Although the K-orthogonality cannot be guaranteed for an unstructured grid, the non-monotonic behavior of the multipoint flux approximation (MPFA) method can cause significant errors, leading to over- or underestimation of pressure and rate values. The files needed for the discretizations and simulation within open-DARTS were provided as preliminary information and follow the uniform Brugge model that is present within the open-DARTS repository. Reservoir and physical properties are assigned to the model in the simulator and presented within Table 3.1.

Property	Value	Units
k	50	[mD]
φ	0.10	[-]
P_{ini}	200	[bar]
T_{ini}	350	[K]
z	2000	[m]
β	$1 \cdot 10^{-8}$	[1/bar]
ρ	1000	[kg/m^3]
μ	0.3	[cP]

Table 3.1: Reservoir properties and physics defined within open-DARTS for the unstructured '5-block' model.

To be able to simulate the well on the unstructured grid, exactly 12 unstructured grid blocks were found directly surrounding the well radius in the mesh. This number can also be deduced from Figure 3.2, thus the obtained number of cells within open-DARTS is consistent with the mesh observed in Gmsh. The additional geometry around the well ensures that the number of neighboring cells stays constant across all future cases and implementations within the model validation process. As a result, the mesh in the proximity of the well will stay unchanged when an exact well position is enforced. The cells that directly border the wellbore are perforated within the simulator, and a large well index (10^{10}) is assigned to these cells. The well is assigned as a producer well and will operate at a constant pressure (P_{prod}) of 150 bar.

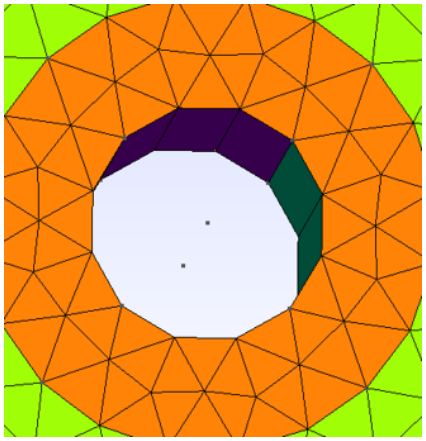

Figure 3.2: The geometrical wellbore, showing the 12 unstructured cells that directly border the well geometry. These blocks are perforated and represent the well within the open-DARTS.

The unstructured model is simulated for a short period of time and uses constant time steps of 10^{-3} days. This is chosen due to the fact that the reservoir only spans a total distance of 300 m in both the x and y directions; therefore, it is not needed to run the model for a long period of time. The pressure response for each cell at each timestep is saved and extracted. Similarly, the flow rate of the well is extracted from the simulation results for each timestep. The unstructured cells that are located within the coarse block containing the well are identified. The pressures at each timestep and volumes of the identified cells are used to calculate the volume-averaged reservoir block pressure for the structured mesh. The volume-averaged well block pressure is defined by

$$\bar{p} = \frac{\sum_i \bar{p}_i V_i}{\sum_i V_i}. \tag{3.1}$$

Subsequently, the average well block pressure and well flow rate are obtained for each timestep. The well index can thus be determined accordingly for each timestep as presented in Equation 3.2;

$$WI = \frac{q^w \mu}{\bar{p} - p^w}. \tag{3.2}$$

To answer the research question, the well index results obtained from the unstructured grid must be verified; hence, they are compared to the analytical Peaceman well index as described in chapter 2. The Peaceman well index is calculated following Equation 2.20 and it should be multiplied by Darcy's constant (c) to ensure translation to the correct units within the open-DARTS framework. Finally, the background grid uses block dimensions of 100 by 100 meters. Therefore, following Peaceman's approximation in Equation 2.20, r_0 will equal a value of 20.8 meters [21].

3.3. Model Verification

The well index for simulation of an unstructured '5-block' model with dimensions 100 by 100 meters and a well positioned at the center position, (150, 150), was calculated following Equation 3.2. This was done based on a constant permeability profile across the reservoir of 50 mD. The Peaceman well index following Equation 2.20 and the dimensions of the reservoir, thus Δx = 100 m, Δy = 100 m and h = 10 m, is 5.4454 $m^3/day \cdot cP/bar$. The well index that is obtained from the unstructured 5-block model, improved well index model, is 5.1608 $m^3/day \cdot cP/bar$, therefore showing the obtained well index being within approximately 5% accuracy of the Peaceman approximation. Later, we will introduce a systematic study to explain the nature of this deviation and discuss several approaches to improve this numerical estimation.

This estimation follows from the solution shown in Figure 3.3. Figure 3.3 shows the well index calculation within the time interval of 0.05 days. This well-indexed value for the unstructured model corresponds to the converged steady-state value. Finally, it is important to mention that when the solution

is run for a longer period of time, and the reservoir approaches depletion, the calculated well index will deviate from this value before ultimately turning to zero. This is further evidenced by Figure B.1 within Appendix B. The exact time at which the latter occurs is highly dependent on the assigned permeability of the mesh.

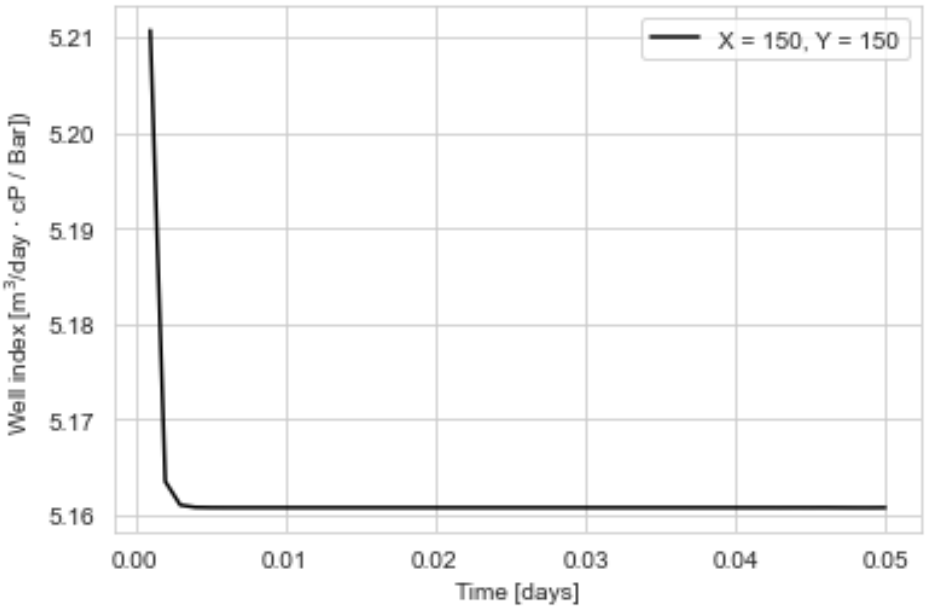

Figure 3.3: Well index curve using a center position for the well (150, 150), following Equation 3.2. The well index is computed for a reservoir with a constant permeability profile of 50 mD.

4

Model Validation

The following chapter will describe the methodology and results for the systematic validation study of the established well index computation method. Firstly, the model is validated for different well placements and permeability profiles. Additionally, the effect of the considered reservoir blocks within the unstructured model is demonstrated. Lastly, the model is assessed against a full unstructured approach for a two-dimensional synthetic reservoir, the 'Egg Model'.

4.1. Well placement

4.1.1. Strategy

The unstructured well index results as a function of well position within the well block are analyzed. This is done by running unstructured models for different well placements with a constant well operating pressure of 150 bar. Well position for the model is changed along either the x- or y- axis, while keeping the other axis at its block-center position of 150 m. It must be noted that the generated model already includes the well and its placement. Therefore, the unstructured mesh has to be regenerated for every case with a different well placement, thereby making the meshes dissimilar. The meshes are created for altering well positions with an increment of 5 meters along either the x- or y-axis. To get a better understanding of how the solution behaves closer to the boundaries of the square grid block, an increment of 0.5 meters is used near the sides of the well block. The well index results are formulated as a multiplier relative to the solution obtained at the center well position going forward, thus relative to the solution obtained at x = 150 m and y = 150 m.

4.1.2. Results

y-axis

The results obtained for the well placement along the y-axis with increments of 5 meters are plotted in Figure 4.1. From the graph, it is observed that the well index behaves mostly symmetric, but not completely. For well positions closer to the boundary of the coarse well block, well index values do not match, and the result tends to be more asymmetrical; closer to the center of the block, solutions yield more identical estimations. Nonetheless, the latter is not the case for the solution with the well placement position (150, 155). The value to which this solution converges is significantly lower than those with well placements (150, 145), (150, 160) and (150, 140). The well position that results in the lowest well index corresponds to the placement (150, 105), the solution converges to a ratio of 0.8376, in other words, indicating a decrease of more than 15% in well index compared to the center well position.

The well index multiplier is also plotted over the y-axis for different solution times. To smooth the curve, a moving average filter is applied and the result is presented in Figure 4.2. The original result can be found in Appendix B. It must be noted that as a result of the moving average filter, the estimations at the edges are lost, as no value can be calculated for the well indices at y = 105 and y = 195, which were present in the original solution. Figure 4.2 shows that for larger elapsed times, solutions will overlay

each other, by these means showcasing the convergence of the well index calculations.

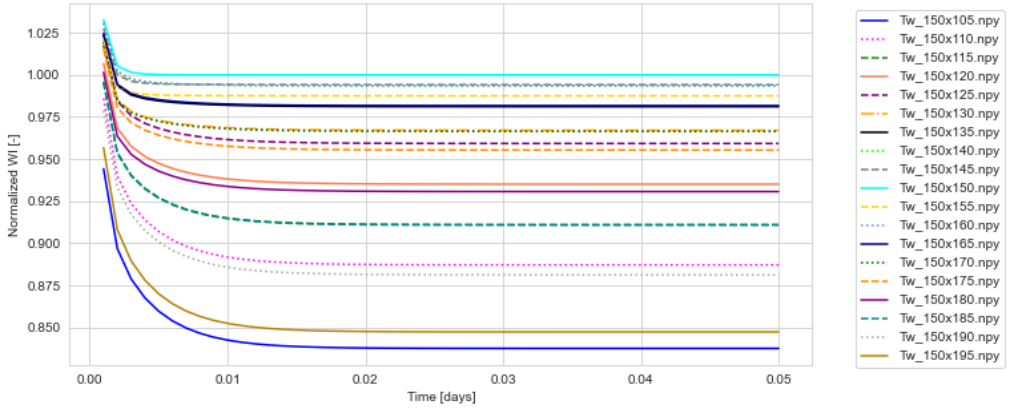

Figure 4.1: Well index for different well positions along the y-axis.

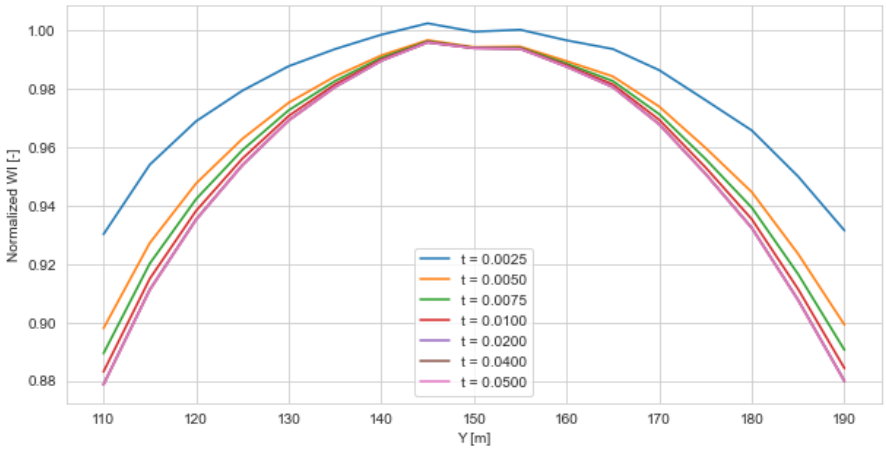

Figure 4.2: Well index as a function of y-axis position for different times. A moving average filter is applied to the graph to smooth variations in well index.

To better analyze the drop-off in well index at the edges of the original grid block, the normalized well index at the top and bottom edges was calculated using a 0.5-meter increment starting from the edge solutions present in Figure 4.1. The sensitivity of the well index over the vertical position in the edges is shown by Figure B.5 in Appendix B. The normalized well index is found to further decrease close to the boundary and reaches a minimum ratio of 0.6387 on the bottom edge and a value of 0.6742 on the top edge. This corresponds to a decrease of 36.13% and 32.58% respectively. Both edges in Figure B.5 show that the solutions at 1 and 2 meters distance from the boundary are slightly higher than those of its predecessor, before decreasing further. Consequently, the solution illustrates non-smooth behavior.

x-axis

The same procedure was performed for the x-axis, and results are presented by Figure 4.3 and Figure 4.4. Results for varying x-axis position of the well show less symmetry than for varying y-axis position. Although differences are small, solutions that lie at the same distance from the center do not necessarily result in the same well index. Nonetheless, the minimum normalized well index lies at 0.8378, and therefore the decrease in well index observed in the x-direction corresponds to that of the y-direction. Finally, the behavior of the normalized well index at the left and right edges of the original grid block was tested. These results are demonstrated in Appendix B by Figure B.6.

The minimum values the normalized well index reaches at the left and right edges are 0.6814 and 0.6897, respectively. This is slightly higher than was observed for the top and bottom edges. These values correspond to a decrease of 31.82% and 31.03% in the well index at the boundaries. Finally,

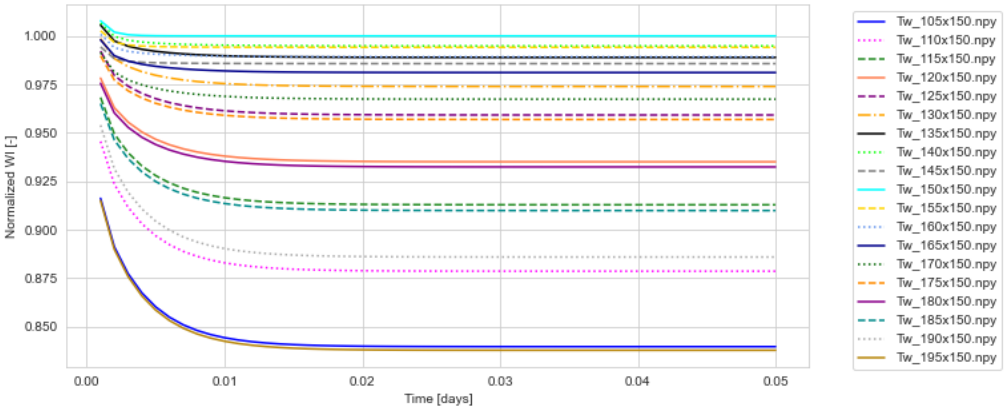

Figure 4.3: Well index response for different well positions along the x-axis.

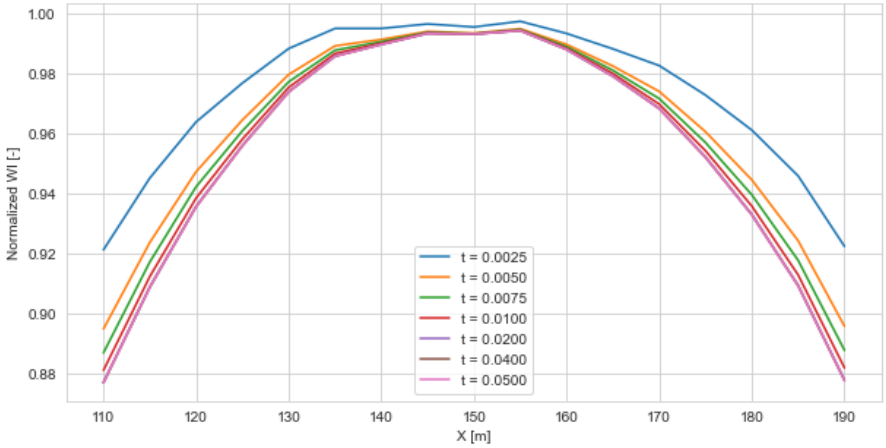

Figure 4.4: Well index as a function of the x-axis position for different times. A moving average filter is applied to the graph to smooth variations in well index.

the results for the x-axis showed a similar non-smooth behavior as for the y-axis. For example, the result at x = 103 m shows a significantly low value for the well index compared to surrounding values.

MPFA discretization

The results using the TPFA scheme in Figure 4.1 and Figure 4.3 do not show smooth behavior over the spatial domain. To check if this is caused by the dissimilarity of the meshes and thus the non-K-orthogonality of the grids introducing discrepancies, the well indices were determined using an MPFA discretization of the unstructured mesh. Due to the similarity in the well index behavior of the x and y axes for the TPFA case, MPFA discretization is only carried out for meshes with moving well positions along the y-axis. The well index multiplier, normalized by the center well index solution, for different well placement positions along the y-axis is plotted, and the results are shown in Figure 4.5.

The lowest observed well index for position (150, 110) reaches a well index ratio of 0.891 relative to the center solution. From Figure 4.5, it is observed that solutions that have the same distance to the center (150, 150) lie on top of each other. Therefore, the solution obtained shows fully symmetric behavior over the y-axis. This is demonstrated more clearly in Figure 4.6. Figure 4.6 shows the expected symmetrical behavior without needing to apply a moving average filter. Nevertheless, the solution at a distance of 5 meters from the boundaries of the well block still yielded asymmetric behavior even when applying the MPFA method. Therefore, a distance of 10 meters from the boundary, corresponding to well placement (150, 110) and (150, 190), was chosen as the minimal distance the well needed to remain from the boundary to not observe any asymmetrical behavior and errors due to boundary effects. This distance is sustained during further validation with the two-dimensional synthetic reservoir and the application to the Geothermie Delft (GTD) reservoir.

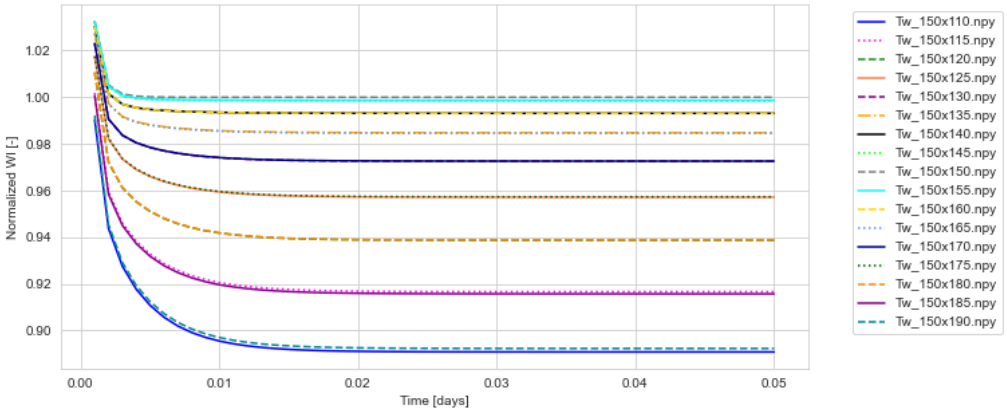

Figure 4.5: Well index ratio results for different well placement positions along the y-axis using the MPFA discretization method.

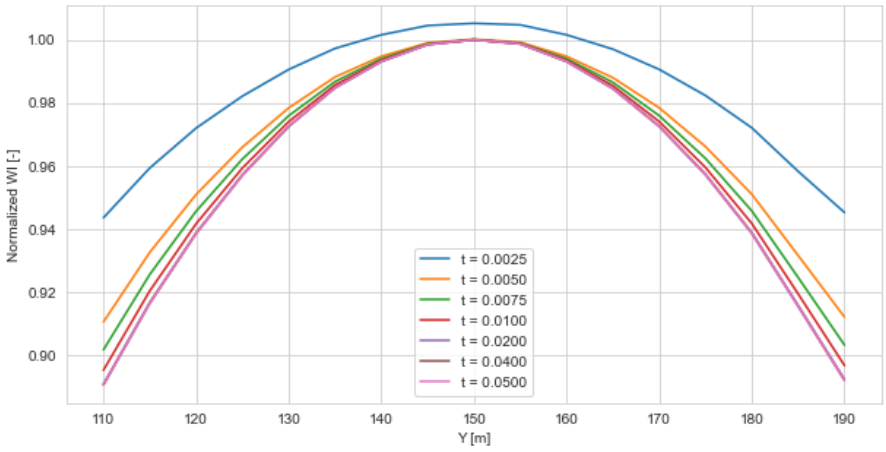

Figure 4.6: Well index as a function of well placement along the y-axis for different times.

4.2. Permeability effect

4.2.1. Strategy

The model was validated for different permeability profiles of the 5-block model, and the following approach was pursued. The permeability of the structured well block, also referred to as k_2, was set at 10 mD. The permeability in the surrounding blocks, k_1, is altered such that the ratio k_1/k_2 changes. For the homogeneous case, the ratio k_1/k_2 is 1. A ratio of 0.1, 1, 10 and 100 is tested to investigate the impact on well index estimations. In Table 4.1, the different tested cases for permeability are presented. The results are presented as a multiplier along the x- and y-axis.

Ratio: k_1/k_2	**k_2 [mD]**	**k_1 [mD]**
0.1	10	1
1	10	10
10	10	100
100	10	1000

Table 4.1: Different ratio's for k_1/k_2 investigated within open-DARTS and their associated permeabilities.

4.2.2. Results

The well index response to altering the permeability of the surrounding blocks is presented in Figure 4.7, which shows the well index as a function of well position y at simulation time t = 0.04 days for the

different permeability relationships. When moving the well closer to the edge, the effect of permeability is felt. Higher permeabilities in the neighboring blocks cause an increase in the well index. For lower permeability in neighboring blocks, the well index decreases even further.

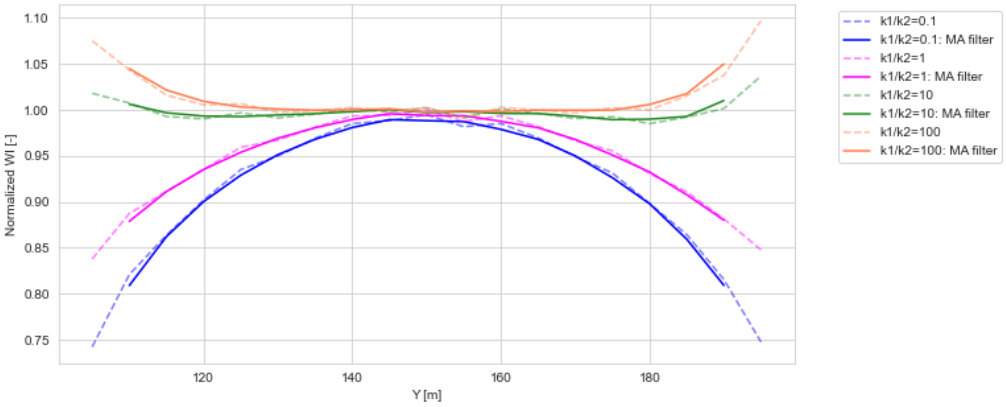

Figure 4.7: Well index as a function of well position y at time t = 0.04 days for different permeability relationships. A moving average filter is applied to filter the results, this is depicted by the solid line in the graph. The unfiltered results are presented using a dashed line.

The graphs for the horizontal x-axis showed identical behavior compared to the y-axis, therefore, this solution is added within Appendix B. To check if the solutions in fact showed equivalent behavior, results are presented in a table, where well index for the center, 150, and two edge positions, 105 and 195, are reported. The non-changing axis was kept constant at a well coordinate of 150 m.

k_1/k_2	y-axis position			x-axis position		
	y = 105 m	y = 150 m	y = 195 m	x = 105 m	x = 150 m	x = 195 m
0.1	0.7412	0.9948	0.7471	0.7455	0.9948	0.7423
1	0.8376	1.0000	0.8475	0.8397	1.0000	0.8378
10	1.0181	1.0023	1.0369	1.0179	1.0023	1.0188
100	1.0753	1.0027	1.0973	1.0745	1.0027	1.0765

Table 4.2: Sensitivity analysis results for the well index over either the vertical or horizontal axis for different permeability ratios.

Results obtained for the sensitivity along the x-axis are fairly consistent with those of the y-axis. Nonetheless, asymmetry is observed mostly in the sensitivity of the well index over the y-axis. The well index on the top edge of the well block is for all permeability cases higher at this location than at the bottom edge, hence showing more variations between the edges than for the x-axis. For the sensitivity results along the x-axis, no asymmetry in values is observed. Final well index values may vary slightly; however, no clear edge returns higher or lower values than the other. The differences between the left and right edges are also to a lesser extent than those between the top and bottom edges. Because these results were obtained using TPFA discretization, MPFA discretization was used similarly as in section 4.1 to examine the asymmetry of the solution.

The results for the permeability effect on well index when using MPFA discretization were obtained and are depicted by Figure 4.8. A minimum distance of 10 meters from the boundaries of the original grid block is kept to avoid interference from the boundary with the solution. Results presented by Figure 4.8 show smooth and symmetric behavior for all permeability ratios without the need of applying a moving average filter. The behavior of the graphs for the different ratios is consistent with that of the TPFA results.

In Table 4.3, a comparison of the resulting well index values between the MPFA and TPFA methods is included. It is observed that well indices calculated by the MPFA method tend to be higher than the TPFA counterparts. However, percentage differences between the two methods do not exceed 1.5%.

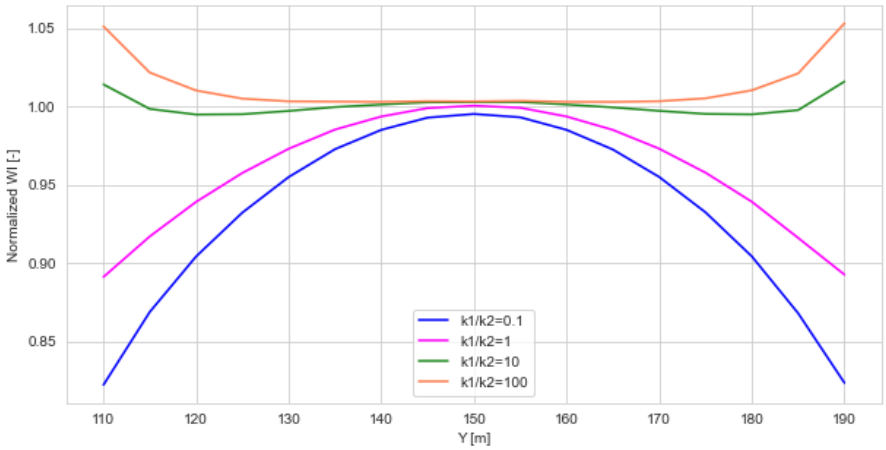

Figure 4.8: Well index plotted over well placement on the y-axis for different permeability ratio's between the center and surrounding 4 blocks.

k_1/k_2	y = 110 m		y = 150 m		y = 190 m	
	MPFA	**TPFA**	**MPFA**	**TPFA**	**MPFA**	**TPFA**
0.1	0.8242	0.8206	0.9952	0.9949	0.8255	0.8152
1	0.8911	0.8872	1.0000	1.0000	0.8926	0.8813
10	1.0140	1.0075	1.0028	1.0023	1.0159	1.0015
100	1.0511	1.0435	1.0032	1.0027	1.0530	1.0377

Table 4.3: Sensitivity analysis results for the well index over the y-axis for different permeability ratios using the MPFA and TPFA schemes.

4.3. Considered number of blocks

4.3.1. Strategy

Finally, a similar well placement and permeability analysis are performed for a reservoir model of nine blocks. This model was built in the same manner as the 5-block model within chapter 3. Ultimately, this reservoir represents a full three-by-three block reservoir. Thus, in other words, the effect of considering four additional blocks on the well index is investigated. The generated mesh corresponding to a '9-block' reservoir is added within Appendix B.

4.3.2. Results

The impact of increasing reservoir size and number of blocks was investigated, since in previous results only a 5-block system has been considered. Firstly, the effect of changing well position is plotted for both the 5-block and 9-block models along the y-axis. The well index multiplier for both models is illustrated by Figure 4.9. Figure 4.9 shows that well index values at the center position are similar; however, when moving closer to the boundary of the well block, the 9-block model returns higher well index values than the 5-block model. For instance, the 5-block system well index took on a value of 0.849 at the top edge, and the extended reservoir at the same edge returns a value of 0.895.

The sensitivity over the y-axis for different permeability relationships was again tested; however, now a 9-block model was employed. The well index results for well indices at time t = 0.04 days are presented in Figure 4.10.

From Figure 4.10 it is observed that values for the well index close to the center of the well block are roughly the same and lie around a similar value as when utilizing a 5-block model. Nonetheless, when moving the position of the well, the effect of the permeability ratios can be observed. Comparing this with the results for the 5-block system in Figure 4.7, it can be seen that values for the well indices of the 9-block reservoir are higher than for the previous system. This was likewise demonstrated by Figure 4.9.

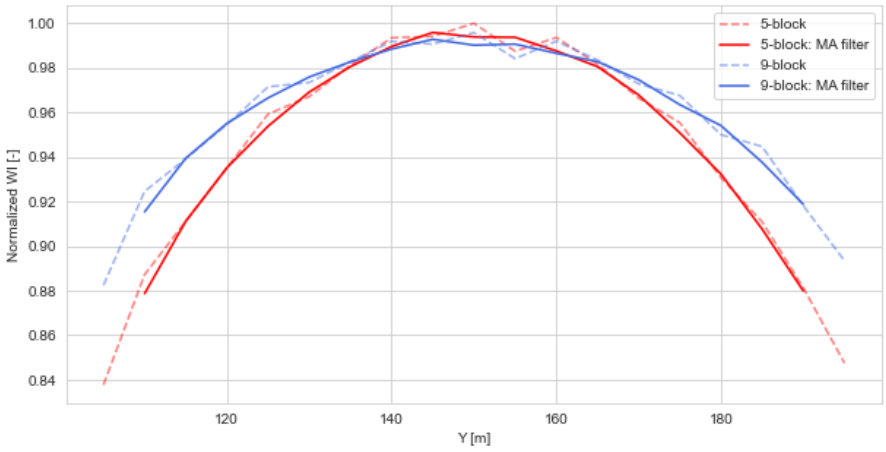

Figure 4.9: Comparison between well indices for the 5-block and 9-block reservoir model using TPFA discretization.

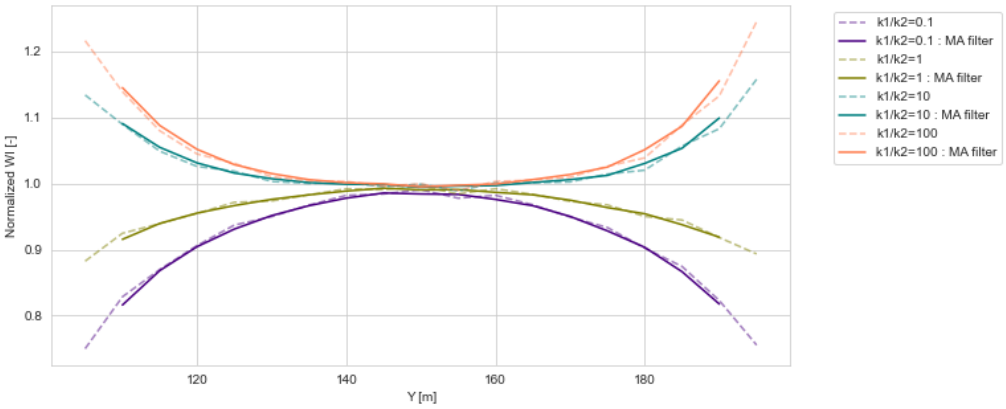

Figure 4.10: 9-Block well indices for different permeability relationships as a function of position along the y-axis.

4.4. Synthetic reservoir Model

The well index model will be validated against a fully unstructured approach for a two-dimensional synthetic reservoir. For this synthetic reservoir model, the 'Egg Model' is utilized [14]. First, the model and applied strategy are elaborated before finally presenting the obtained results.

4.4.1. The 'Egg Model'

The 'Egg Model' is a synthetic reservoir that contains a total of 100 three-dimensional permeability realizations [14]. The realizations describe the stochastic model of a channelized reservoir, and each realization contains 60 x 60 x 7 grid blocks. Additionally, each realization shows a strong vertical correlation, which makes the realizations almost two-dimensional. In Figure 4.11, four random permeability realizations are presented that are included within the 'Egg Model'. It must be noted that within the model, permeability in the x-direction is equal to that in the y-direction. Moreover, the presented realizations are two-dimensional because they correspond to the 4th out of 7 vertical layers (i.e., z is fixed at the 4th cell). The two-dimensional slices are shown in Figure 4.11 for different realizations.

Realization 9 was selected to move further with due to the presence of multiple channels in the reservoir's center, a feature shared by several other realizations in Figure 4.11. However, the final choice was made somewhat arbitrarily from among the realizations exhibiting this characteristic. The strategy will further be explained according to realization 9, and results are generated for this specific permeability realization. Nevertheless, the method is generally independent of the permeability realization, and permeability realizations can easily be interchanged. The dimensions of the 'Egg Model' were reduced by cropping the model to a smaller version with 20 x 20 x 7 grid blocks. This is done to maintain acceptable run times for the model, as the results will be compared to fully unstructured simulations.

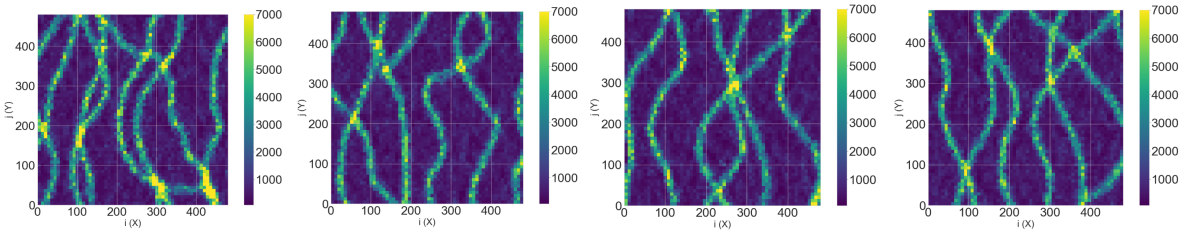

(a) Realization 5 **(b)** Realization 9 **(c)** Realization 17 **(d)** Realization 19

Figure 4.11: Four random permeability relationships included within the 'Egg Model'. The realizations are two-dimensional, where z is taken equal to the 4th reservoir layer.

Therefore, a total of 20 blocks are cut off at each boundary of the reservoir. Additionally, the objective for the synthetic model is a well index map of nine blocks located in the center of the reduced permeability realization. The well will be moved through these 9 blocks, and utilizing local well index calculation, well index estimations for each well position in these 9 blocks will be calculated. This will be further explained in the following sections. The nine-block region is referred to as the well index investigation area. In Figure 4.12, the reduced synthetic reservoir is presented for realization number 9 at each layer z. The well index investigation area is marked within the realization by a red square. Within Figure 4.12, it is observed that layer 4 shows the largest range in permeability values, and the heterogeneity within the well index investigation area is more significant than in the other layers. This finding was established through the calculation of the Lorenz coefficient for each layer in the realization shown in Figure 4.12 [4]. The Lorenz coefficient is a descriptor that interprets the degree of heterogeneity of a reservoir property, where zero indicates a homogeneous system and 1 corresponds to a completely heterogeneous system. The results are captured within Figure 4.13. From Figure 4.13 it can be deduced that layer 4 holds the largest Lorenz coefficient, specifically 0.4992. Thus, indicating this layer contains the largest degree of heterogeneity. Hence, layer 4 is chosen as the permeability profile to simulate within open-DARTS.

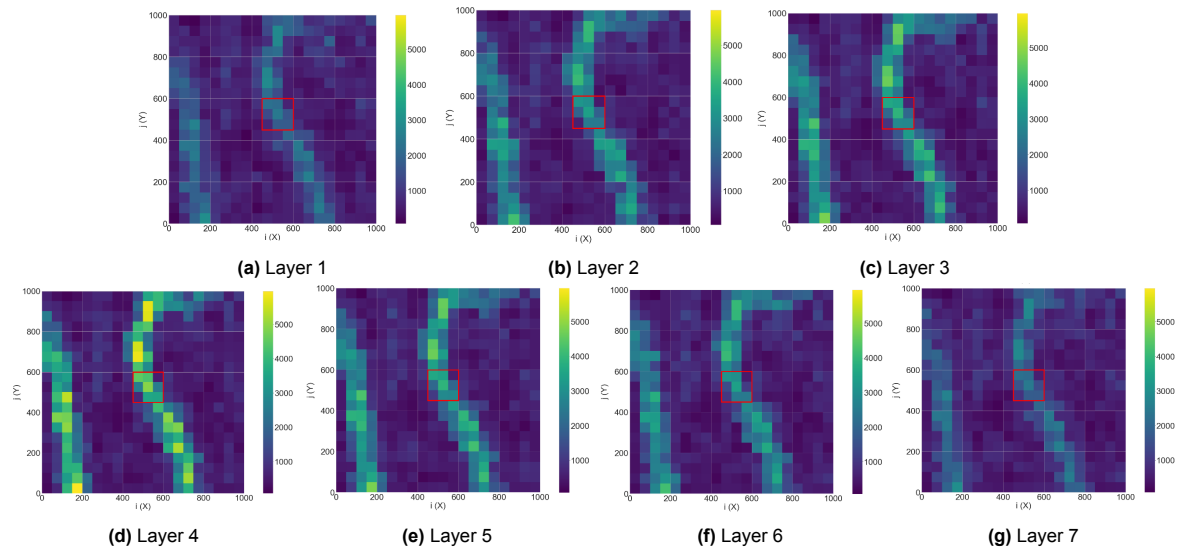

(a) Layer 1 **(b)** Layer 2 **(c)** Layer 3

(d) Layer 4 **(e)** Layer 5 **(f)** Layer 6 **(g)** Layer 7

Figure 4.12: The reduced permeability realization for realization 9, the WI investigation area is included and is marked by the red square. All 7 layers in the z-direction are included.

Lastly, the original dimensions of the 'Egg Model' are defined as: Δx = Δy = 8 m and Δz = 4. However, if the reduced reservoir version is used combined with these dimensions, the total reservoir length in the x and y-direction will only be 160 m. Therefore, the cell dimensions, e.g., Δx and Δy are set to 50 m moving forward. Thus, resulting in a total reservoir size of 1000 meters in the x- and y-direction. The model will now cover a larger total physical area, but will contain fewer grid blocks. Furthermore, because Δz is kept constant, the ratio of lateral and vertical scale changes.

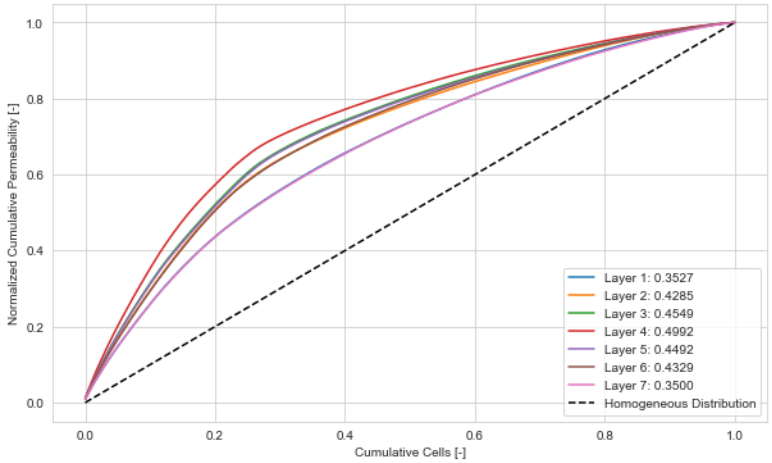

Figure 4.13: Flow capacity distributions for every layer within Figure 4.12, the Lorenz coefficient for every layer is computed and was added within the figure legend.

4.4.2. Strategy

Within this section, the strategy for rigorous well-index validation is briefly described.

Meshing

For the validation of the well index model against a full unstructured approach, an unstructured mesh is created. Within Gmsh, the full unstructured mesh is created by first building the 20 by 20 grid block structured case, matching the dimensions of the 'Egg Model'. The well is added following the same strategy as used to model the well for the well index model, thus by adding two cylindrical geometries. One cylindrical shape aligns with the radius of the well, while the other cylindrical shape has a radius of $r_{well} + 0.1$. Moreover, in the central 10 by 10 blocks, a finer unstructured grid is applied; the remaining sections of the reservoir were modeled with a coarser grid. The following characteristic lengths or mesh resolutions were set for the full unstructured mesh:

- The characteristic length is 0.1 at the well,
- The characteristic length is 0.1 at the second cylindrical geometry at a distance of 0.1 from the well,
- The characteristic length was set to 5 at the boundaries of the central structured 10 by 10 blocks,
- A characteristic length of 20 was specified at the boundaries of the remaining structured blocks.

A reservoir thickness h of 4 meters was used to match the thickness of a single layer within the 'Egg model'. Multiple well placements within the well index investigation area are considered to observe how the well index changes as a function of placement. Therefore, meshes are generated for increments of 5 meters within the well index investigation area and with a minimal distance of 10 meters from the boundaries of the structured grid cells. A single resulting mesh for a random well placement within the well index investigation area for the full unstructured mesh is depicted in Figure 4.14.

Well index calculation

Multiple types of simulations are performed within open-DARTS to obtain values for the well indices in the area of interest. The full unstructured reservoir is simulated to determine well indices; similarly, the improved well index model is employed to compute well indices. Within the well index model, different numbers of included blocks are considered when determining estimations. Well index values for the full unstructured grid are calculated by utilizing the same technique as was used for the well index model, namely by use of Equation 3.2 and Equation 3.1. Note that the reporting time step and production bottom hole pressure that were used for the theoretical reservoir, namely $1 \cdot 10^{-3}$ and 150 bar, are likewise used to model the full unstructured reservoir. Similarly, fluid properties stay constant over the considered models.

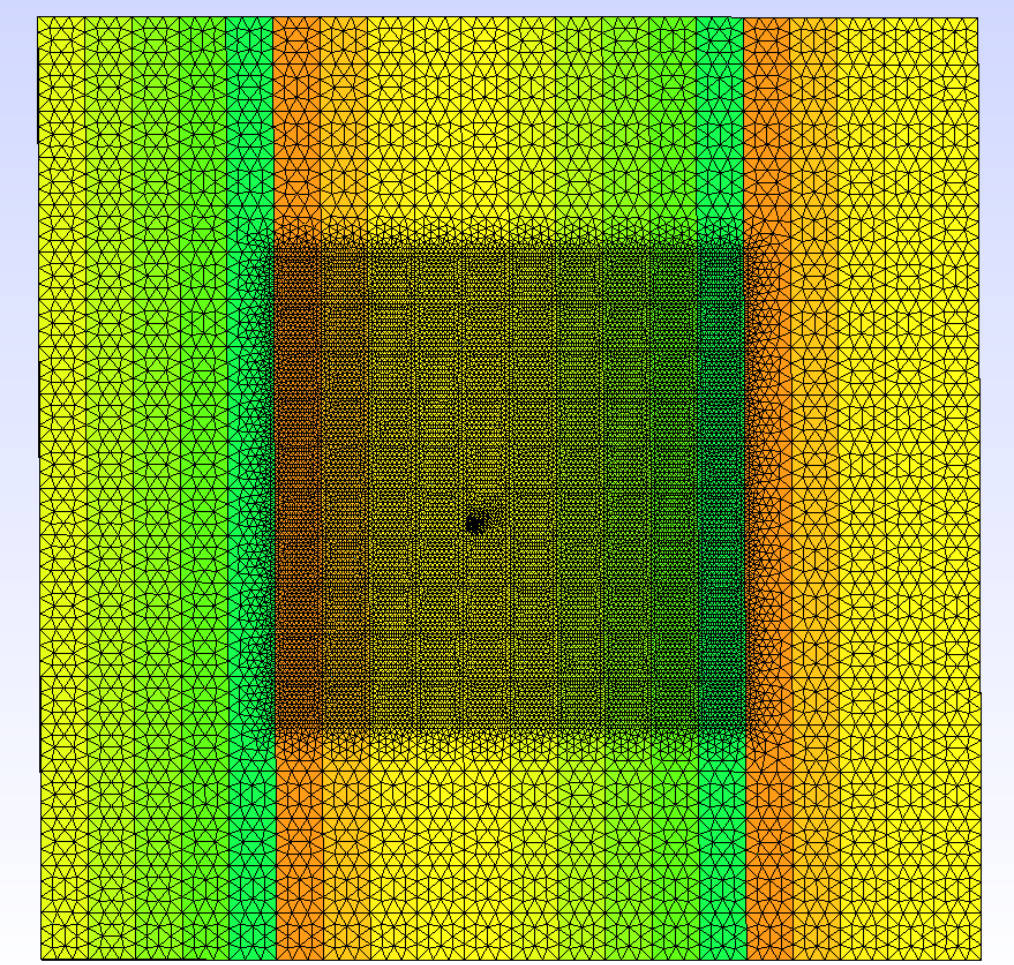

Figure 4.14: Resulting mesh following the mesh strategy for the synthetic reservoir model, well placement is located within the well index investigation area. Dimensions of the reservoir correspond to 1000 by 1000 meters.

Firstly, the full unstructured reservoir was simulated for a total of 49 well positions in each reservoir block of the well index investigation area. The empty mesh is filled with the permeability values following the chosen realization of the 'Egg model'. The full reservoir is simulated, and the volume-averaged well block pressure is returned. Well indices are then obtained by following Equation 3.2. For well index determination using the established well index model, the approach looks slightly different. For every block within the well index investigation area, the adjacent blocks are found. The permeability of the chosen well block is assigned to the center block in the empty mesh; the surrounding blocks of the empty mesh are filled with the permeabilities of the matching neighboring blocks within the 'Egg model'. Thus, the permeability profile that is assigned to the mesh contains only local permeability and differs depending on the reservoir block in which the well is located. Based on the simulation outcomes from the improved model, well indices are determined.

The results for the simulated cases will be presented in a pointwise map. The pointwise maps are compared to each other by closely analyzing the spatial well index behavior. Finally, the impact of using MPFA discretization is investigated, and the performance of the MPFA discretization is compared to the TPFA approach.

4.4.3. Results

Peaceman well index

The permeability map for the well index investigation area and the surrounding ring with reservoir blocks is plotted to obtain a better insight into the permeability profile in the proximity of the area of interest. As depicted earlier, the investigation area is located at one of the channels of realization 9. This was cho-

sen specifically to include significant permeability changes between the cell blocks. The permeability profile is included in Figure 4.15.

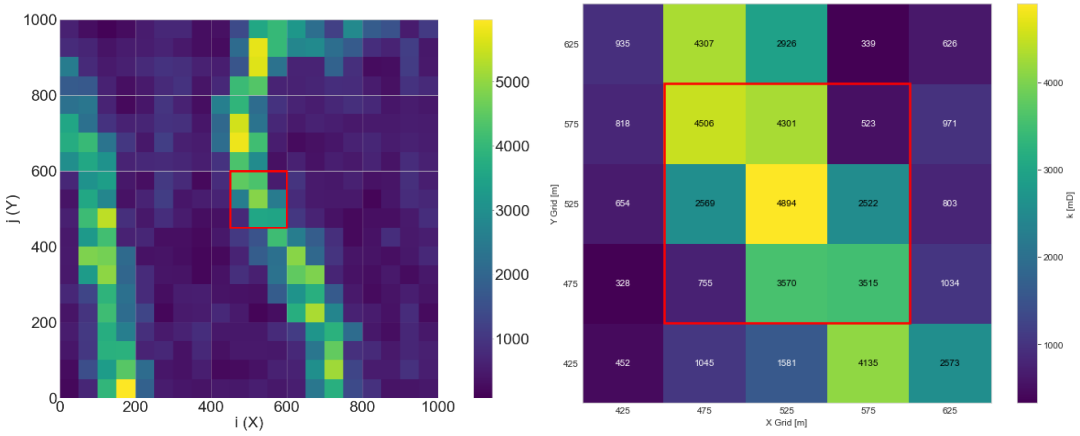

(a) Full profile **(b)** Close up profile

Figure 4.15: The full permeability profile (a) and the close up permeability profile for the well index investigation area and the ring with neighboring blocks (b).

The Peaceman well indices for the reservoir blocks that belong to the well index investigation were calculated using Equation 2.20. These were used to firstly validate the range of results; moreover, they allow for error quantification, thus showing how far full and unstructured model results lie from each other. The results for the analytical well index calculation are presented in Table 4.4. From the table, the range of well indices for the area of interest is observed and falls between 26.5 and 248.2 $m^3/day \cdot cP/bar$.

Block index	k [mD]	WI [m^3/day · cP/bar]
(11, 9)	4506	228.50
(11, 10)	4301	218.10
(11, 11)	523	26.52
(10, 9)	2569	130.27
(10, 10)	4894	248.17
(10, 11)	2522	127.89
(9, 9)	755	38.29
(9, 10)	3570	181.03
(9, 11)	3515	178.24

Table 4.4: Permeability and equivalent analytical well index of the well index investigation area following Peaceman's approximation.

Full unstructured results

Well indices were calculated for 49 points in each reservoir block of the well index investigation area and are based on the full unstructured reservoir solution as presented in Figure 4.14. Table 4.5 presents the well index results for every block at its center.

Values generated by the fully unstructured grid match the range of values following from the analytically calculated values. However, the values do all lie lower than the Peaceman's counterpart. Nevertheless, all center block values achieved by the full unstructured method lie within 7 to 9% error compared to Peaceman's formula. To observe how the well index values change when the well is moved *off-center*, a pointwise well index map is generated and included within Figure 4.16. Figure 4.16 shows the variability of the well indices over the lateral dimensions within the blocks of the well index investigation area.

Variability in well indices can be observed for the middle block of the investigation area, which shows symmetric behavior of the well index over the dimensions of the block. Other blocks within the investigation area, however, do not all exhibit this symmetry. In particular, blocks such as those in the upper

left and lower right corners demonstrate asymmetric well index distributions, where lateral well index behavior is influenced by neighboring permeability contrasts. In blocks with low permeability variability contrasts appear less pronounced, this is also in part due to the visual representation in Figure 4.16, where the associated low well index values are displayed with dark blue colors, thereby weakening the visibility of subtle variations.

Block index	Center coordinates [m]	WI [m^3/day · cP/Bar]	Error in WI [%]
(11, 9)	(475, 575)	208.81	8.6%
(11, 10)	(525, 575)	200.52	8.1%
(11, 11)	(575, 575)	24.49	7.7%
(10, 9)	(475, 525)	119.20	8.5%
(10, 10)	(525, 525)	228.12	8.1%
(10, 11)	(575, 525)	117.67	8.0%
(9, 9)	(475, 475)	35.41	7.5%
(9, 10)	(525, 475)	165.47	8.6%
(9, 11)	(575, 475)	162.97	8.6%

Table 4.5: Well index results for the full unstructured mesh. The block index and center well position for each block are given together with the obtained well index from the fully unstructured model. The normalized error in the well index calculation against the analytical Peaceman well index is shown to check the accuracy of the center well index values.

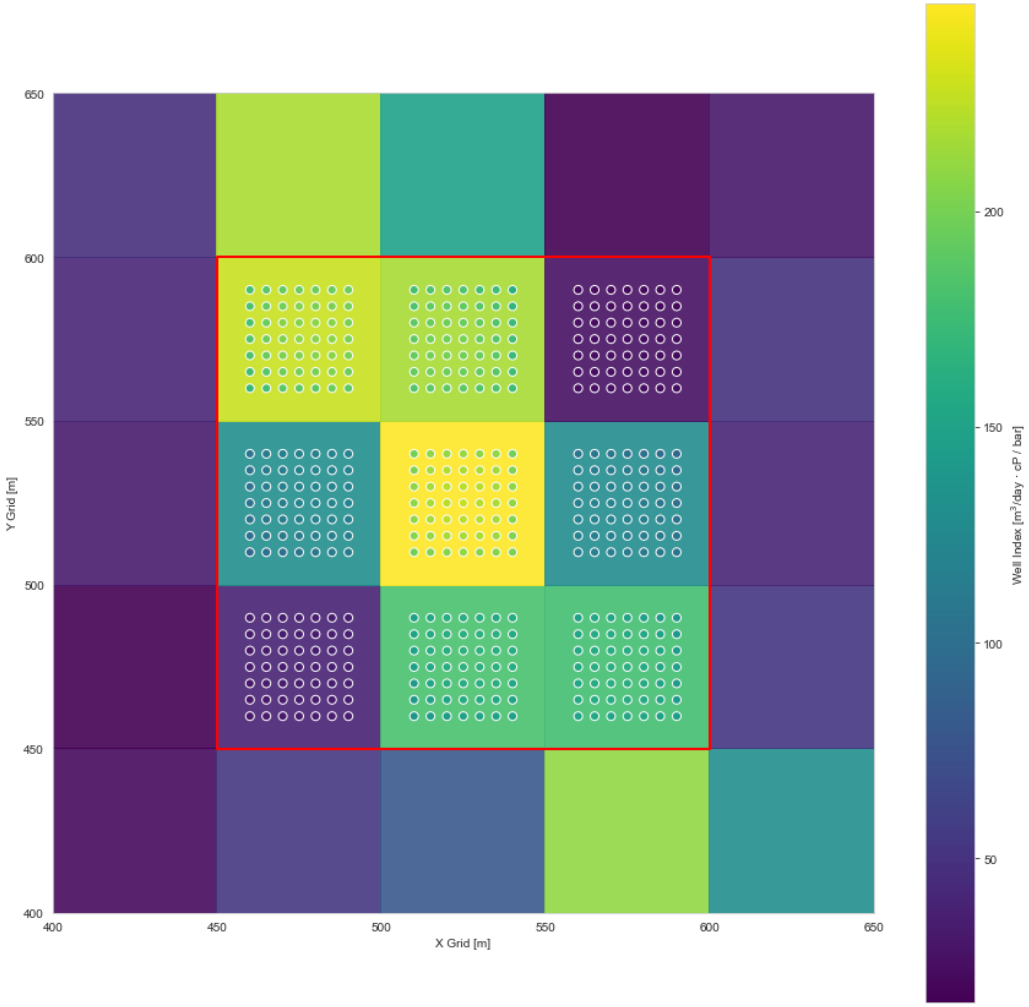

Figure 4.16: Well index results for the full unstructured approach within the investigation area. Background color indicates well indices from the analytical Peaceman formula.

5-Block results

The well index model is applied on the well investigation area, and the obtained well index results are presented in Figure 4.17. Figure 4.17 also includes the normalized error of the 5-block result with the full unstructured result. Furthermore, well placements that showed high errors have been marked by a circle within Figure 4.17b. These points were used to further analyze the behavior of the error between the full unstructured approach and the well index model.

Figure 4.17a and Figure 4.16 do not show the same well index pattern and present significant differences in well indices in certain blocks, especially towards the boundaries with neighboring blocks. This is especially evident from Figure 4.17b, but can also be observed within Figure 4.17a, particularly in the top left and top center blocks, where the patterns in well index behavior are more symmetric than in Figure 4.16. Furthermore, the 5-block method shows lower resulting values for the well indices, and the general pattern is that the largest well index is observed at the center of the blocks. Finally, the normalized error between the two methods reaches values up to 10%, with high errors observed at the block boundaries.

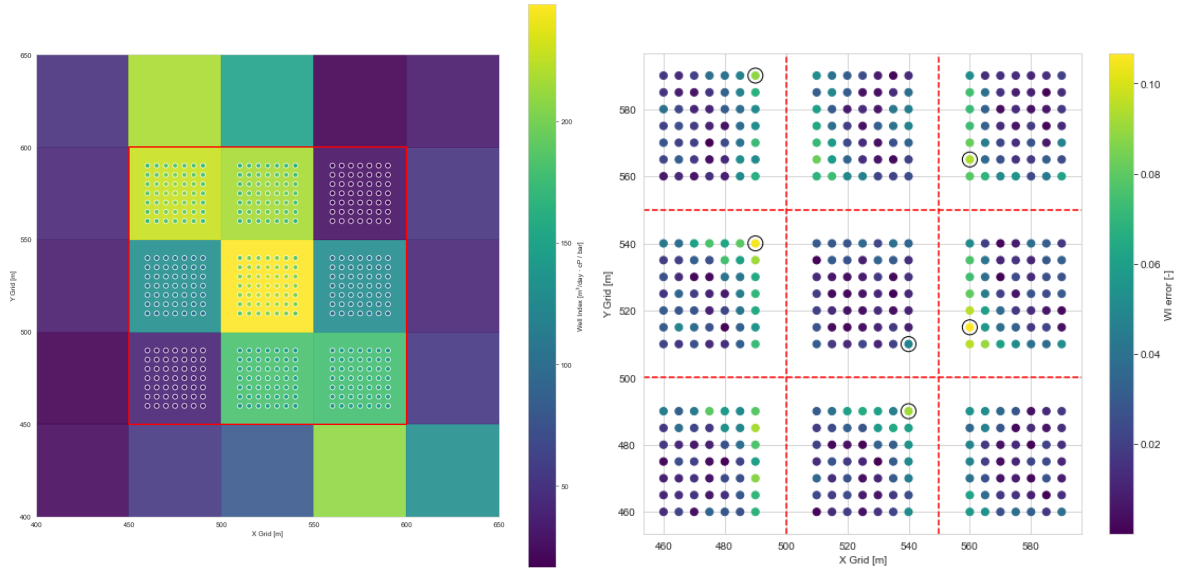

(a) WI solution **(b)** Normalized WI error

Figure 4.17: Results for the 5-block method for evaluating the well indices within the investigation area (a) and the normalized error in well indices between the 5-block method and the full unstructured method is plotted accordingly (b).

9-Block results

The well index model is extended to a 9-block scheme, which takes into account the permeability profile of the corner blocks that are not present in the 5-block models. The effect of incorporating more reservoir blocks on the evaluated well indices is tested, and well index results are depicted in Figure 4.18a. The calculated well indices are higher than the 5-block method, hence resulting in smaller normalized differences between the 9-block and full unstructured method, as can be observed by Figure 4.18b. Normalized errors between the full unstructured approach and the 9-block model have decreased up to a maximum of 6%. The pattern of the full unstructured solution can be better recognized in the 9-block result than in the 5-block result; nevertheless, the solution obtained by the 9-block method is deemed insufficient. Therefore, the effect of using MPFA was investigated, as well as the addition of another layer to the mesh and thus resulting in a '25-block' well index model. The results from MPFA indicated an improvement in performance regarding the assessment of well indices, thereby slightly closing the gap between the full unstructured approach and alternative proposed methods. The resulting maps for the MPFA discretization are included in Appendix B (Figure B.8 and Figure B.9). Well index values are further compared to the TPFA method in Figure 4.4.3.

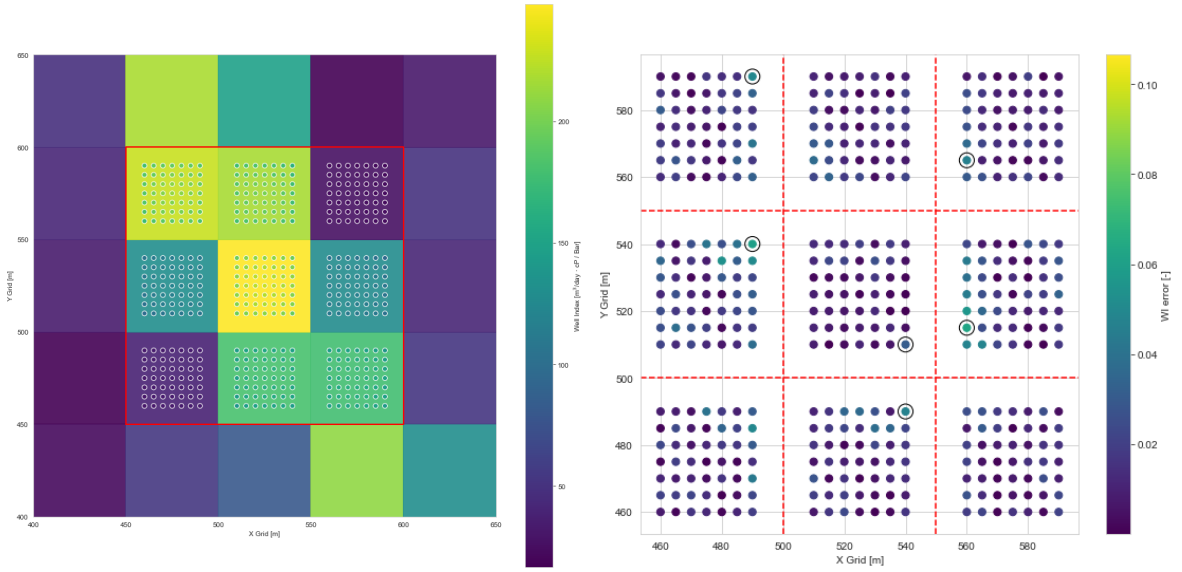

(a) WI solution **(b)** Normalized WI error

Figure 4.18: Results for the 9-block method for evaluating the well indices within the investigation area (a) and the normalized error in well indices between the 9-block method and the full unstructured method (b).

25-Block results

The 9-block result was deemed closer to the full unstructured model evaluations but still introduced an error around 6% for a few locations. Therefore, an additional 25-block case was tested. Furthermore, MPFA discretization exhibited better well index outcomes in both the 9-block and the 5-block case. Therefore, the 25-block case was exclusively tested following the MPFA discretization method in open-DARTS. The well index map solution for the 25-block case is presented in Figure 4.19. The attained solution resembles the full unstructured approach than in the situations involving 5 and 9 blocks. Discrepancies between the 25-block case and the full unstructured model have decreased below 4%.

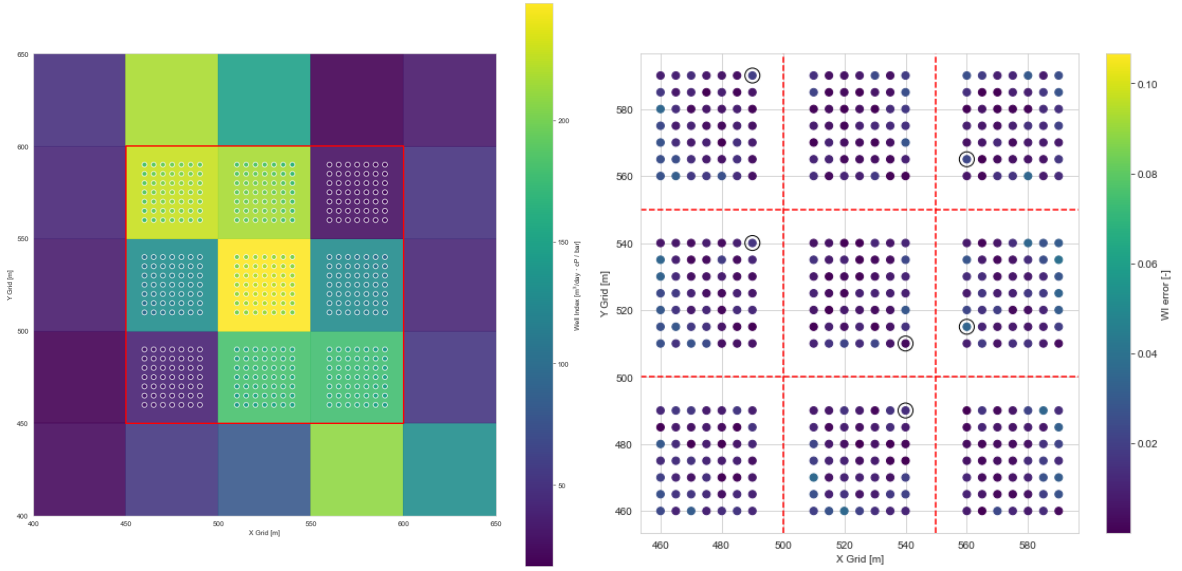

(a) WI solution **(b)** WI error

Figure 4.19: Solution for the well index map using a 25-block approach and MPFA mesh discretization. The full solution (a) and an normalized error map with the full unstructured result (b) are both displayed.

Method and discretization comparison

The well index results obtained for each method and each discretization method are summarized below in Table 4.6, a total of six well positions were chosen. These positions were selected because they demonstrated large discrepancies between the complete unstructured approach and the initial 5-block model. These points correspond to the circled well placements within the obtained normalized error plots (Figure 4.17b, Figure 4.18b and Figure 4.19b). To better visualize Table 4.6, a graph is presented in Figure 4.20, illustrating the behavior of the normalized error for different included placements within the well index model.

Well position	**Method**	**WI [$m^3/day \cdot cP/bar$]**	
		TPFA	**MPFA**
(560, 515)	Full unstructured	118.68	118.28
	5-block	105.05	106.20
	9-block	110.69	111.83
	25-block	-	114.31
(540, 510)	Full unstructured	201.55	202.62
	5-block	189.72	193.17
	9-block	193.86	197.51
	25-block	-	200.81
(560, 565)	Full unstructured	25.65	25.53
	5-block	23.17	23.41
	9-block	24.43	24.66
	25-block	-	25.03
(540, 490)	Full unstructured	157.97	159.31
	5-block	141.31	144.37
	9-block	149.39	152.72
	25-block	-	155.42
(490, 540)	Full unstructured	117.96	120.06
	5-block	104.34	106.54
	9-block	110.20	112.67
	25-block	-	115.80
(490, 590)	Full unstructured	196.35	196.99
	5-block	176.10	179.85
	9-block	184.97	189.06
	25-block	-	191.85

Table 4.6: Well index comparison for different chosen placements, and the TPFA and MPFA discretization. The chosen well placements showed large normalized errors between the full unstructured approach and the well index model.

Ultimately, the main takeaway from Table 4.6 and Figure 4.20 is that the more reservoir blocks are considered for the mesh, the closer the solution gets to the result of the full unstructured grid. Additionally, MPFA discretization does generate better results, because differences between the full unstructured result and the other methods stay smaller than when making use of TPFA discretization. Finally, full unstructured grid results show that the discrepancy between the TPFA and MPFA methods remains little and only for well placement at coordinates (490, 540), a significant difference between the two approximations is recognized.

Performance comparison

Performances of the simulator are compared for the different applied methods, including the different discretization techniques. To achieve this, the total elapsed simulation time in seconds for the well located at coordinates (460, 460) is recorded for every scenario. The results are presented in Table 4.7. Performance results show that TPFA discretization is more than twice as fast in comparison to MPFA discretization. Furthermore, increasing the reservoir size considered in the unstructured mesh increases simulation runtime likewise. The 5- and 9-block runtimes are quick, and runtimes of the full

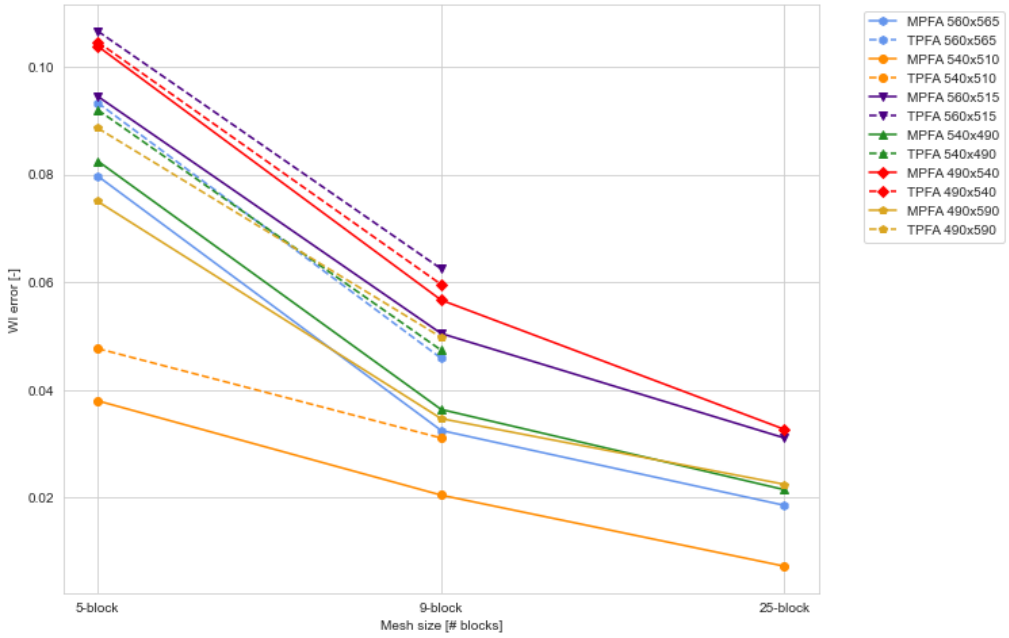

Figure 4.20: Graph showing the decrease in normalized well index error when considering more blocks within the well index model compared to the unstructured approach.

unstructured mesh are acceptable; however, it is important to point out that initializing the mesh, especially that of a full unstructured reservoir, takes more time compared to the other evaluated methods. This adds to the performance of the initialization stage for the reservoir model.

Method	Discretization	
	TPFA	MPFA
Full unstructured	3.2191	8.6542
5-block	0.1317	0.3402
9-block	0.2559	0.5684
25-block	-	1.4694

Table 4.7: Total elapsed simulation time in seconds for well position (460, 460) for every performed method.

5

Reservoir application

5.1. Geothermie Delft Project

The final application of this study will be on the Geothermie Delft (GTD) doublet. Therefore, the following paragraphs will describe the project and the target reservoir thoroughly. The geological context and characteristics of the target reservoir will be discussed in more detail before the simulation strategy and results are presented.

In 2023, two geothermal wells were successfully completed at the Delft University of Technology campus. The geothermal project was originally named the Delft Aardwarmte Project (DAP); however, the commercial name that is currently utilized is Geothermie Delft (GTD) [10, 12]. The project is planning to start heat production for the university campus and the surrounding built environment in 2025. The target formation for the geothermal project is the Delft Sandstone member, which resides within the Nieuwerkerk Formation [31]. The Niewerkerk formation represents the Schieland group within the West Netherlands Basin (WNB) and primarily consists of continental sediments, with the Delft Sandstone Member containing thick sand packages. Figure 5.1 depicts a sample of the well log of the producer well for the GTD project, the sample includes gamma ray, resistivity, sonic, neutron density and porosity, and nuclear magnetic resonance.

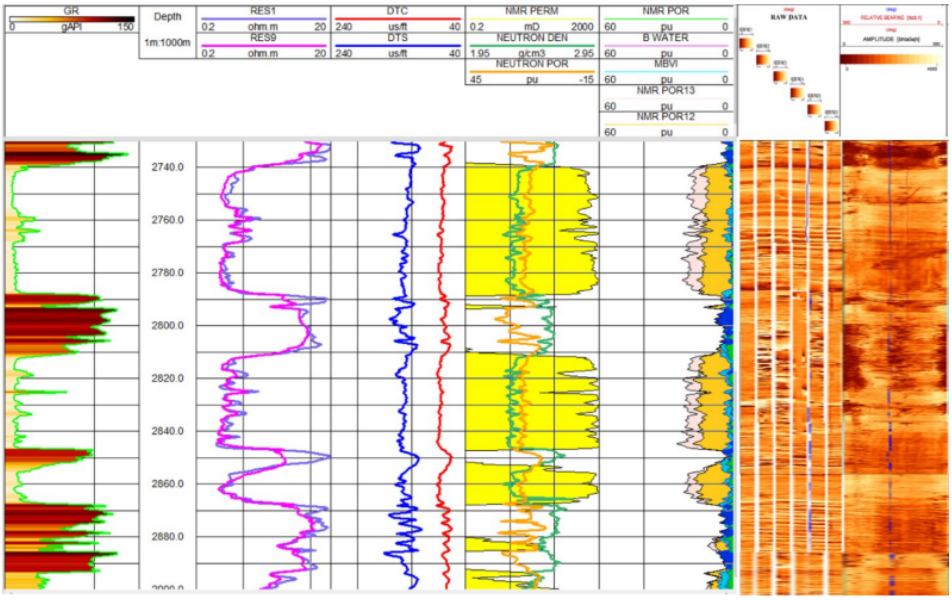

Figure 5.1: Portion of the well logs of the producer well (DEL-GT-01) for the GTD project at reservoir depth. Multiple logs are presented, including gamma ray, resistivity, sonic, neutron density and porosity, and nuclear magnetic resonance [28].

Sandstones of the Delft Sandstone member formed in a humid, lower-coastal-plain meandering environment [31]. The target reservoir lies conformably on top of the Alblasserdam Member and is overlain by the Rodenrijs claystones. Within the Niewerkerk formation, three units with different net-to-gross ratios are defined. These are presented by Figure 5.2, the figure also shows the gamma ray response of the three respective units. Intervals predominantly containing medium to high net-to-gross units are currently identified as the Delft Sandstone Member.

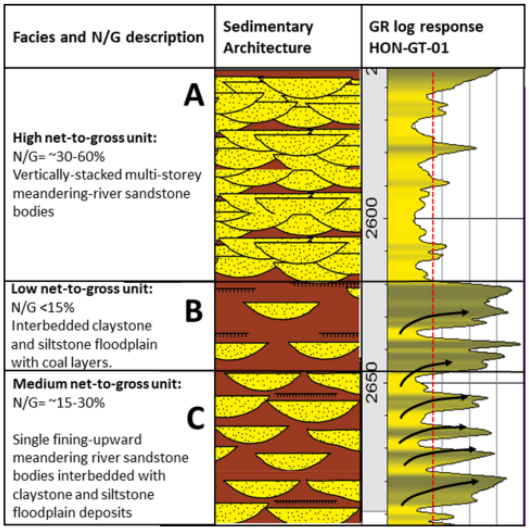

Figure 5.2: The three units defined within the Niewerkerk formation, the three units contain different net-to-gross ratios and gamma ray signatures [31].

The GTD reservoir is located within a syncline and is bounded by two faults. One of which is at approximately 1 km distance, whereas the other is located at a distance of 4 km from the surface location [28]. The geothermal doublet wells (DEL-GT-01; producer and DEL-GT-02-S2; injector) have depths ranging from approximately 2 to 2.5 kilometers. Both wells are deviated such that deeper and hotter parts of the reservoir can be reached, and the distance to the closest fault increases. The properties of the reservoir are characterized accordingly: the porosity of the Delft Sandstone Member ranges between 8% and 25%, while the corresponding permeability spans from several mD to as much as 3000 mD [31]. Finally, the project will deliver hot water at a temperature of 80°C and has a maximum thermal energy extraction rate of approximately 25 MWth [28].

5.1.1. Reservoir model

The reservoir model characterizes the GTD reservoir and is made up of 112x112x100 cells. Each grid-cell is an approximate dimensions of Δx = 50 m, Δy = 50 m and Δz = 1 m. Additionally, the attained model only contains porosity values as a reservoir property. Therefore, to acquire permeability values for the reservoir, a relationship is needed between porosity and permeability. In this context, the relationship introduced by Willems et al. [31] is utilized to find permeability values. This correlation is derived from measurements and collected plugs from wells. The correlation between porosity and permeability is defined by

$$\begin{aligned}\log_{10}(k_D) = -3.523 \cdot 10^{-7} \cdot \varphi^5 + 4.278 \cdot 10^{-5} \cdot \varphi^4 - 1.723 \cdot 10^{-3} \cdot \varphi^3 \\ +1.896 \cdot 10^{-2} \cdot \varphi^2 + 0.333 \cdot \varphi - 3.222.\end{aligned} \tag{5.1}$$

Furthermore, the original exact well trajectories are given for the producer (DEL-GT-01) and injector (DEL-GT-02-S2) wells, as well as the discretized well trajectory containing well positions at the centers of the perforated structured cells and corresponding porosity values [28]. The raw well trajectory contains coordinate values approximately every 10 meters.

5.2. Simulation strategy

To calculate well indices for the GTD model according to the established well index model, first, intersections between the reservoir cells and the true well trajectory are found. Based on the intersection points, meshes are generated accordingly. Lastly, when the correct meshes are obtained, the 5-block and 9-block well index models are used to estimate accurate well index values. This is performed for both wells within the geothermal doublet, namely DEL-GT-01 and DEL-GT-02-S2.

5.2.1. Well trajectory intersections

The GTD reservoir model is formulated in CPG format, which allows the CPG discretizer in open-DARTS to return the following characteristic arrays:

- `face_nodepos`: This array tells at which index in the `face_nodes` array a certain face starts. This array allows us to deduce the number of nodes and which nodes make up a certain face.
- `face_nodes`: This index array describes the node indices that make up a face. Combined with `face_nodepos`, the start and end indices are defined, and the corresponding node indices are found.
- `node_coordinates`: The array contains the coordinates of each node. Together with `face_nodes`, the coordinates of the points making up a face can be found.
- `face_cells`: This array contains the cells that are being connected by each face, or in other words, the cells that are adjacent to every face. For boundaries, the cell index -1 is returned.

For each face in `face_nodepos`, the `face_nodes` array and `node_coordinates` array are combined to find the node coordinates that describe each face of the reservoir. For each segment of the well trajectory, intersections with the face are found using a plane-line intersection algorithm, where the plane and well trajectory are described as vectors in three-dimensional space. Lastly, when an intersection is found, the cells that are adjacent to this face are extracted using the `face_cells` array, the second cell index is used which is returned by `face_cells`. Subsequently, the intersections, cell index (i, j, k) and face centers are extracted for each intersection, such that the meshes can be built accordingly.

5.2.2. Mesh generation

Meshes for the 5-block and 9-block model are built in Gmsh using the obtained intersections, cell indices and face centers. Meshes are created similarly to earlier established meshes, such as within section 3.1 and subsection 4.4.2. The structured blocks within the meshes have dimensions Δx = Δy = 50 m, corresponding to the dimensions of the GTD model. Additionally, layer thickness Δz is set to 1 m. The layer thickness of Δz = 1 m was assumed for both the numerical and theoretical models. This assumption was based on the initial available information and provided a practical and robust starting point for mesh generation and model development. However, to further improve the physical accuracy of the model, actual values of Δz can be extracted from the simulation grid by analyzing cell centroids or node coordinates from the earlier described arrays. Lastly, meshes are generated for each intersection by calculating the difference between the face center and the intersection, assuming a flat plane. A minimal distance of 10 meters from the cell block boundary is installed within Gmsh; this assumption was based on the MPFA validation results. Therefore, wells that are within a distance of 10 meters of the block boundary are modeled as they are located at the minimal distance of 10 meters.

5.2.3. Well index estimations

Once each mesh for each intersection is created, the cell indices corresponding to each mesh are extracted. These indices are utilized in detecting the assigned well block, enabling the identification of the permeability profile of the well block and its neighboring blocks in the spatial two-dimensional plane (k is set constant). The permeability profile is assigned to the mesh, and the simulation is run for the local model; a reporting timestep of $1 \cdot 10^{-2}$ was used for the simulation. Nevertheless, all other parameters were kept unchanged. It must be noted that permeability values of zero or close to zero were encountered; these were handled by setting them to a value of 1 mD. Well indices for the meshes are determined, and the multiplier was found by normalizing the well indices based on Peaceman's model, which is used to determine normalized error values for the applied methods.

5.3. Results

The results of the proposed well index calculation in application to the GTD wells and a comparison of the simulation results with those obtained using Peaceman's formula are reported within the following section.

5.3.1. DEL-GT-01

Intersections between the well trajectory and the reservoir cells were found, and the obtained well trajectory can be observed below in Figure 5.3. A full overview of the intersection points, cell indices and face centers is included within Appendix B. The well indices for each cell intersected by the well trajectory were identified using the Peaceman model, which assumes a center well position. Determined values for the well indices along the well are included within Figure 5.3. The well index behavior following Peaceman's approximation appears categorical; this is due to the geologic model, which describes only a high-permeable sand or low-permeable shale, thus eliminating large parts of internal variation. Cells with lower permeability show a degree of variability in both permeability and the resulting well index. Nonetheless, all reservoir cells identified as permeable sandstone consistently have a well index value of 26.04 $m^3/day \cdot cP/bar$ for perforated reservoir cells.

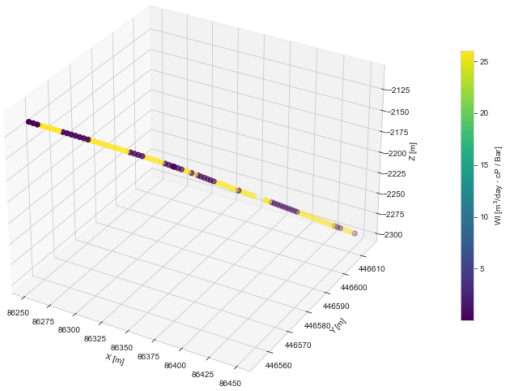

Figure 5.3: Well indices for the cells penetrated by the well trajectory based on the Peaceman approximation.

Figure B.10 contains the intersections starting at the top of the Delft Sandstone reservoir until the well leaves the target formation. Results show the well is generally continuous, except for a small disruption towards the end of the well. This disturbance corresponds to reservoir cell layers k = 64 and k = 65, and at these cell layers, no intersections with the well trajectory were found.

5-block approximation

In Figure 5.4a and Figure 5.4c, the well index results and normalized errors are depicted along the well's vertical length using a 5-block approximation, with further representations available in Appendix B. The result shows the same pattern in high-low values as the Peaceman case. Note that for the well index solution presented in Figure 5.4a and Figure 5.4c only values are present for the reservoir cells containing sandstone; additionally, both the estimated well indices and the Peaceman indices are included in Figure 5.4a. Within the new approach, more variation in the well index is observed than was present in the reference Peaceman well solution. Figure 5.4c shows the normalized well index error for all computed cells. The normalized well index value plot illustrates that computed well index errors stay between 0 and 30%. The normalized error is taken relative to the Peaceman well index. Higher normalized error values can be observed throughout the entire well, but are often observed at points where the well moves into a block with different i or j position compared to the previous block. This occurs at depths of roughly 2140, 2239, and 2282 m following Table B.1. Lastly, block thicknesses are not constant within Figure 5.4. The thick block between 2225 and 2250 meters depth corresponds to the missing intersections at k = 64 and k = 65, thin blocks correspond to intersections being close in z-value, which mostly occurs when transitioning to a cell with a different i or j position compared to the previous block.

9-block approximation

The well index results using a 9-block estimation for the DEL-GT-01 well are presented in Figure 5.4b and Figure 5.4d. The solutions again show only cells containing sandstone; the Peaceman solution is also included within the figure of Figure 5.4b. Figure 5.4b shows that the obtained solution shows less categorical behavior than the reference Peaceman solution, especially for permeable sandstone layers. The 9-block outcome shows well index values to be closer to each other than for the 5-block approach. Similarly to the 5-block case, the positioning of both high and low well index values is consistent with the Peaceman solution. Lastly, the normalized well index solution within Figure 5.4d shows that returned errors stay above 5%. The largest observed normalized well index error possesses a value of 27 %, which is lower than the maximum error value observed for the 5-block model.

(a) WI solution: 5-block **(b)** WI solution: 9-block **(c)** Error: 5-block **(d)** Error: 9-block

Figure 5.4: Computed well indices and normalized well index errors for the DEL-GT-01 well using both a 5-block and 9-block model.

5.3.2. DEL-GT-02-S2

The attained intersections for the reservoir and the DEL-GT-02-S2 well are shown in Figure 5.5. Figure 5.5 contains intersections for all reservoir layers and thus has no interruptions, unlike the DEL-GT-01 well. Similarly to the DEL-GT-01 well, Figure 5.5 contains the well index solution following the Peaceman well inflow model. The same categorical behavior and similar well index values as for the DEL-GT-01 well were found. It is interesting to note that the axes in Figure 5.5 are rotated; this is due to the well trajectory position for the DEL-GT-02-S2 well being fairly constant along the x-axis. Lastly, a full overview of the well intersections, including cell indices and face centroids, is included within Appendix B.

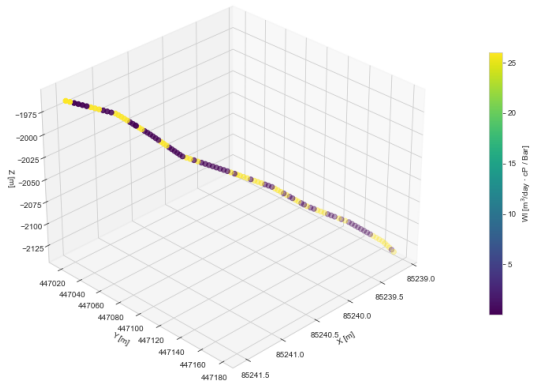

Figure 5.5: Well indices for the reservoir cells penetrated by the well trajectory based on the Peaceman well model.

5-block approximation

Figure 5.6a and Figure 5.6c depict the well index estimations for the DEL-GT-02-S2 well, based on the simulation results for the 5-block model. Both the true solution and the normalized well index errors are shown. The same pattern of high and low well index values is observed in Figure 5.6a as found using the Peaceman model in Figure 5.5. The well index error values do not show a clear pattern and vary throughout the well. The highest observed value for the normalized error corresponds to a value of 35%. This corresponds to the most significant variance between the Peaceman well index and the 5-block well index. In some cases, the well index obtained by the 5-block model is almost equal to that obtained by the Peaceman formula.

9-block approximation

Within Figure 5.6b, the results for well index estimation using a 9-block unstructured model for the DEL-GT-02-S2 well are presented. Results observed in Figure 5.6b present the obtained well index pattern correctly as resolved by Figure 5.5. Similarly to the DEL-GT-01 9-block case, well index values show a smaller spread than the 5-block estimations. Minimum and maximum values of the normalized well index error in Figure 5.6d correspond to 12 to 30%, respectively. Again, the solution derived from the 9-block model demonstrates smoother trends in well index values, unlike the 5-block model, which exhibits some abrupt fluctuations in these values. The changes between the 5- to 9-block are not systematic and vary from location to location.

In terms of computational performance for both the DEL-GT-01 and DEL-GT-02-S2 well, the simulation time for the 5-block model lies around approximately 0.75 seconds, whereas the 9-block model requires around 1 to 1.5 seconds. These times however only include the pure simulation time of one realization along the well for the GTD reservoir and do not account for the intersection calculations and the initialization stage of the reservoir model.

(a) WI solution: 5-block **(b)** WI solution: 9-block **(c)** Error: 5-block **(d)** Error: 9-block

Figure 5.6: Computed well indices and normalized well index errors for the DEL-GT-02-S2 well employing both a 5-block and 9-block model.

5.3.3. Simulation Results

The well indices from the 5-block and 9-block well index model were utilized to simulate the full GTD reservoir model with open-DARTS. It is noted that for the missing intersections in the DEL-GT-01 well, Peaceman well indices were used to simulate the reservoir. Results for the production temperature and bottom hole pressure were obtained; these results are illustrated by Figure 5.7. Additionally, pressure and temperature profiles along both the injector (DEL-GT-02-S2) and producer (DEL-GT-01) wells were acquired. The pressure profiles for the producer and injector wells are illustrated in Figure 5.8 and Figure 5.9, respectively. Temperature profiles of the wells are included within Appendix B in Figure 5.10 and Figure 5.11.

Firstly, it is noted that the production well temperature remains identical over time across the three different cases. However, the bottom-hole pressure shows quite some deviations when comparing the improved well index model to the Peaceman model, where both the 5-block and the 9-block model behave equivalently. Figure 5.8 and Figure 5.9 show the pressure distribution along the production and injection wells over time for the three modeling approaches. Initially, for short simulation times, all models match. However, as the simulation progresses, the improved well index models (5-block and 9-block) reveal variations in pressure along the well. The Peaceman approach generally shows a smoother well pressure behavior for both wells, while the 5- and 9-block models capture more fluctuations in the well pressure. Although the pressure profiles for the producer well (DEL-GT-01) are consistent between the 5- and 9-block models, the injector well (DEL-GT-02-S2) exhibits slight differences between the two. This deviation is vital for data assimilation using real dynamic data from a fibre-optic monitoring system installed along these wellbores [28].

Lastly, temperature profiles along the wells in Figure 5.10 and Figure 5.11 show that the temperature profiles are almost identical except for a discrepancy corresponding to missing well intersections (k = 64 and k = 65) in the production well (DEL-GT-01).

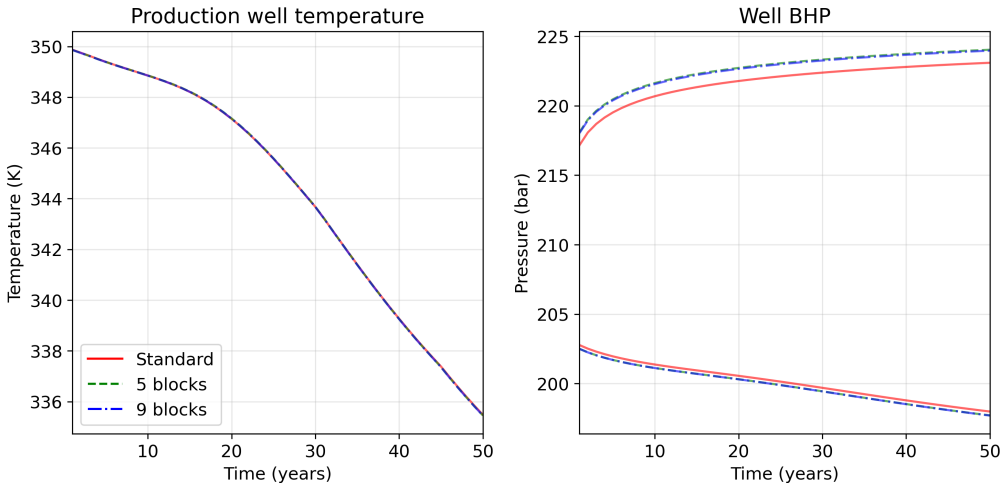

Figure 5.7: Production well temperature and bottom hole pressure for simulation of the GTD reservoir simulation model with the improved well index model and Peaceman's approach.

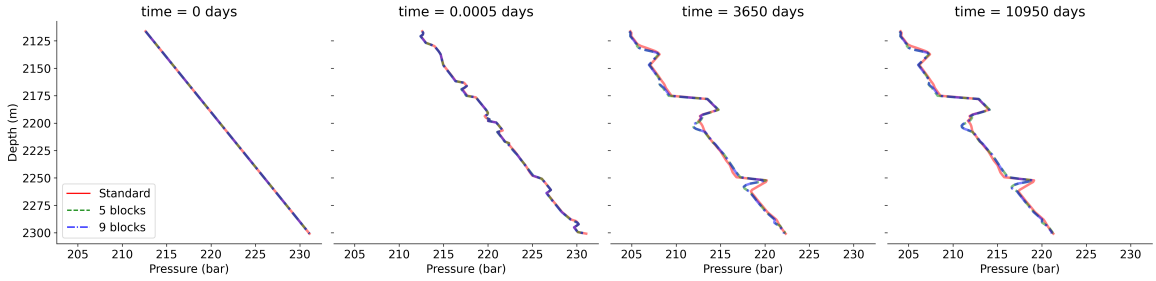

Figure 5.8: Well pressure profile of the producer well, DEL-GT-01, after different times.

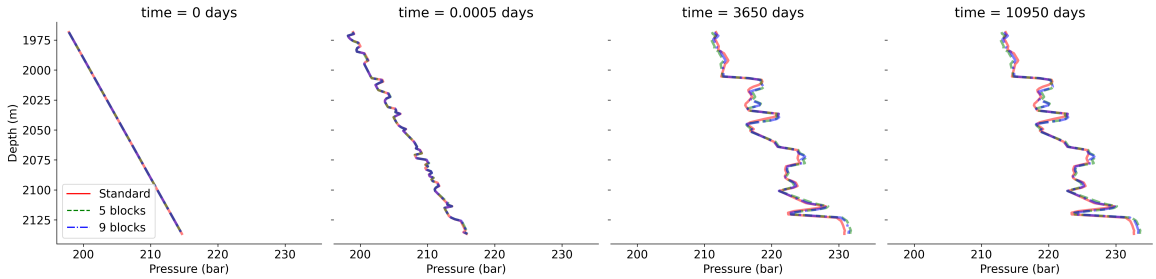

Figure 5.9: Well pressure profile for the injector well, DEL-GT-02-S2, after different times.

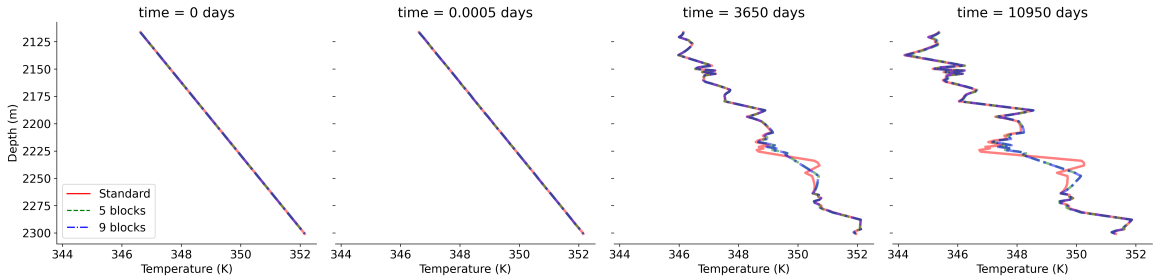

Figure 5.10: Well temperature along the producer well, DEL-GT-01, after different simulation times.

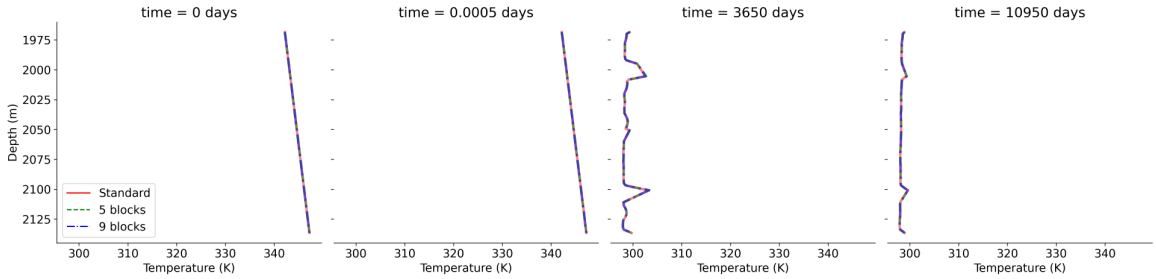

Figure 5.11: Well temperature along the injector well, DEL-GT-02-S2, after different simulation times.

6

Discussion

Verification of the well index (WI) model based on an unstructured modeling approach showed that the model can determine well index values that, at the center location, match those of the Peaceman well model within a 5 % accuracy. This illustrates that the improved well index model yields values within the same range as the Peaceman well index model. This error can be further reduced by using more supporting neighboring blocks and MPFA discretization.

Validation of the well model to a full unstructured approach showed that considering more reservoir blocks within the improved well model leads to a closer resemblance and lower errors with the full unstructured solution. Compared to the 5-block model, the 9-block model provides well indices closer to those obtained from the full unstructured model. Incorporating more blocks additionally yielded consistently more accurate values. These observations give the insight that when more reservoir blocks are considered in the improved well index model, the well index behavior is more accurately captured, and the model can approximate a full unstructured solution better.

Although the scale of reservoir heterogeneity is defined before incorporating the well model within the reservoir simulator, it still influences the computed well index values. That is because the improved well index model relies on the defined permeability profile of the well block and the surrounding lateral blocks for its calculation. Model validation indicated that when high permeability was present in neighboring blocks and low permeability characterized the well block, well indices near the boundaries exhibited higher normalized well indices compared to those located at the center. Conversely, when low permeability values prevail in surrounding blocks and high permeability in the well block, well indices near the boundary of the well block become lower. It is significant to note that the current well index model only includes the two-dimensional permeability profile when evaluating well indices, assuming no-flow boundaries in the vertical direction. This assumption can be influenced by the vertical heterogeneity of the reservoir. Besides, the influence of well inclination may lead to additional inaccuracies. Therefore, extending the model to integrate vertical heterogeneity and well inclination could improve the accuracy of the well index estimations further.

The validation results showed that using a TPFA discretization of the grid introduces errors within the well index estimation. The curves investigating well index behavior over the x- and y-axis exhibited a non-smooth decline of the well index when utilizing a TPFA discretization. This is because meshes generated for every well position are not strictly K-orthogonal and these inaccuracies vary among unstructured meshes generated for different positions. This was further proved by the results obtained using MPFA discretization. These results were indeed smooth over the dimensions of the grid block, hence not showing the same deviations when using TPFA discretization. On closer comparison between the two discretization methods within Table 4.6, it was deduced that errors for the TPFA method remained limited, and well index values for MPFA and TPFA remain close.

Similarly, validation of the model to the two-dimensional synthetic reservoir showed that MPFA only slightly improved the accuracy of estimated well index calculation. Therefore, the TPFA discretization method was still opted for throughout the rest of the research. Firstly, because the TPFA technique is

computationally faster. Secondly, the MPFA method can produce non-monotonic solutions and introduce uncertainties in the systematic well index evaluation. Although TPFA is computationally faster, it must be said that the MPFA discretizer stays within acceptable runtimes and does not hinder the overall simulation workflow, thus still making it a practical option within the spatial unstructured grid discretization of the improved well index model.

Application of the well index model to the GTD wells included finding the exact intersections between the well trajectory and the reservoir layers. The algorithm used to identify these intersections failed to detect intersections for two vertical k-layers, k = 64 and k = 65, in the case of the DEL-GT-01 well. In both layer numbers 63 and 66, the well position of the raw well trajectory is located close to the corner and boundaries of the structured grid block. This follows from Table B.1 in Appendix B. Furthermore, between k = 63 and k = 66, a transition occurs where one well segment ends and another begins, which may have contributed to the algorithm skipping the two intermediate k-layers. When implementing computed well index values in the simulation of the full reservoir, the missing values corresponding to these layers were taken equal to Peaceman's well index. Another approach could be to use an interpolation approach, or take the value equal to its predecessor as displayed by Figure 5.4. For this case, the well indices for the missing layers would thus correspond to the value of reservoir layer k = 63.

The results presented for the GTD model, and more specifically values that were obtained within Figure 5.4a, Figure 5.4b, Figure 5.6a and Figure 5.6b follow from the simulation results and are subsequently extracted for a constant time across all the performed simulations. For instance, in the 5-block model, the time was set to 0.15 days, and for the 9-block model, the value for the extraction time was 0.25 days. Firstly, it is noted that this value is not constant across the two methods. This choice can be explained by the reservoir size and permeability profile. For the 9-block case, the simulated reservoir is slightly larger and has a more complex permeability profile.

As a result, convergence for these solutions takes longer than for the 5-block case; hence, a later time was used to extract well index values. Similarly, for the 5-block reservoir, permeability profiles containing high values for multiple blocks result in the reservoir being drained relatively fast. For the 5-block case, some simulations resulted in complete reservoir drainage occurring in less than 0.25 days. Consequently, all simulations for a given case exhibited varying convergence times, which additionally introduced uncertainty in the extracted well index values when using a constant extraction time. By this stage, certain low-permeability realizations had barely reached convergence, and in some extreme cases, had not converged fully yet. Conversely, high-permeability realizations were nearly completely drained and approached unstable behavior. In summary, the extraction time used to determine well index values can unintentionally introduce errors if not selected appropriately. An example where the above-mentioned case generates errors is further described below.

For both the DEL-GT-01 and the DEL-GT-02-S2 wells, there are realizations that produce an unexpected well index behavior over time at first glance. The graphs over the total defined runtime do not necessarily show convergence. Realizations that show this specific behavior mostly correlate to a permeability profile that possesses a high-permeability well block, but low-permeability adjacent blocks. An example of such a case is observed for the DEL-GT-02-S2 with cell index i = 41, j = 73, k = 94. The corresponding permeability profile and obtained solution under defined timing parameters are depicted in Figure 6.1.

The simulation result associated with the permeability profile in Figure 6.1 does not exhibit the expected shape or convergence toward a single value. However, when the timing parameters are adjusted, particularly when the simulation duration is extended, the correct behavior appears. For this specific case, the resulting solution is shown in Figure 6.2.

Since well indices are extracted at t = 0.25 days for the 9-block case, the example within Figure 6.1 and Figure 6.2 illustrate how this can lead to underestimation of the well index values. While the solution eventually converges to a value of 21.6479 $\mathrm{m}^3/\mathrm{day} \cdot \mathrm{cP}/\mathrm{bar}$, the method captures a lower value of 21.0225 $\mathrm{m}^3/\mathrm{day} \cdot \mathrm{cP}/\mathrm{bar}$ at the specified extraction time, resulting in an error of 2.89 % for this case. Similar underestimations are observed for certain realizations in the DEL-GT-01 well and when applying the 5-block method. Furthermore, for realizations with contrasting permeability profiles, convergence can be slow as well, which in cases can lead to overestimation in a likewise manner. An

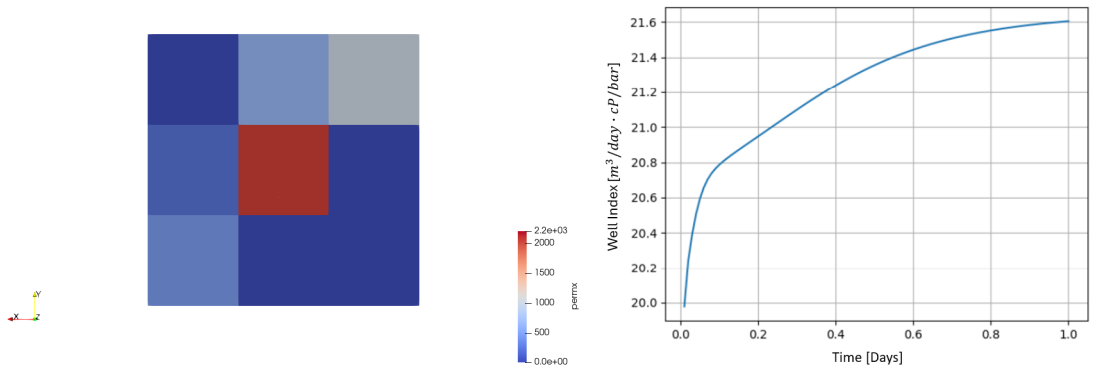

(a) Permeability profile

(b) Simulation solution

Figure 6.1: The permeability profile of reservoir block with index (41, 73, 94) for the DEL-GT-02-S2 well in the 9-block case (a) and the obtained solution following simulation in open-DARTS with the defined timing parameters.

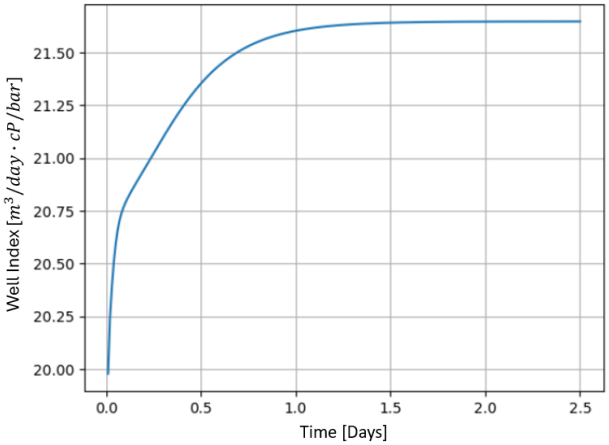

Figure 6.2: Solution showing convergence for well realization in block (41, 73, 94).

example of overestimation for the DEL-GT-01 well is included in Appendix B in Figure B.16. Under- or overestimations can be avoided by adapting the simulation time, detecting the convergence of the steady-state well index.

Ultimately, results following the 5-block approach significantly differ from those obtained with the 9-block unstructured model. Well index results acquired by the 5-block model generally show higher estimated values for sandstone layers. For instance, within the DEL-GT-01 well at the interval between 2170 m and 2180 m (Figure 5.4a and Figure 5.4b) and in the final 20 meters of the DEL-GT-02 well (Figure 5.6a and Figure 5.6b). However, this is not the case everywhere, so are higher well index values for the sandstone layers observed in the 9-block method at the interval between roughly 2140 m and 2160 m of the DEL-GT-01 well and the top part up until 2000 m in the DEL-GT-02-S2 well. Overall, the two methods generate distinct profiles for the well indices of the GTD wells; however, the 9-block method tends to yield values with less variability than the 5-block model.

Based on the validation study on the two-dimensional synthetic reservoir, the 9-block model demonstrated enhanced performance in approximating the well index values compared to a fully unstructured approach, suggesting it offers a more accurate representation of reservoir and well index behavior. On the contrary, while the validation study using the synthetic two-dimensional reservoir showed that the 9-block method tends to produce consistently higher well index values compared to the 5-block method, this trend is not observed in the GTD wells.

An example of this behavior is the calculation of the well index for k = 33 and k = 34 in the DEL-GT-01 well. The 9-block model returns values of 21.9060 and 22.4707 $m^3/day \cdot cP/bar$ respectively, while

the 5-block returns values of 25.2862 and 25.7054 $m^3/day \cdot cP/bar$ for the same layers. Permeability relationships of these layers demonstrate that both layers concern a high permeability well block with adjacent low permeability blocks (Figure B.17). Therefore, this discrepancy may stem from differences in reservoir geometry or heterogeneity, especially because the permeability values of adjacent blocks in the GTD model go lower than in the tested two-dimensional synthetic validation model.

Additionally, it is recognized that the 9-block solutions had not yet fully converged at the extracted simulation times, unlike the 5-block results, which did show convergence of the steady-state value. This may partially explain why the 9-block results are lower; however, it is unlikely that this causes the entire discrepancy. Nonetheless, further research is thus necessary to determine the underlying source of this divergent behavior.

The computed well indices were utilized to simulate the full GTD reservoir model, in contrast to the Peaceman's estimates. From the results obtained within Figure 5.4a, Figure 5.4b, Figure 5.6a and Figure 5.6b, it is evident that well index estimates acquired by the improved well index model are significantly lower in amplitude than the Peaceman well model. The effect on the simulation results of the GTD reservoir was studied by comparing the full simulation results with each other. These results showed that the production well temperature is equivalent for all cases. However, pressure profiles along both the producer and injector wells reveal clear differences between the standard Peaceman model and the improved well index approach, especially for later simulation times.

Additionally, the Peaceman showed smoother pressure distribution behavior than both the 5- and 9-block models. This difference in behavior reflects the improved model's ability to resolve pressure at a finer scale, which the Peaceman model smooths over. Thus, highlighting the enhanced accuracy of the improved well index approach. Although production well temperature is similar for all models, the shape of the cold front was not evaluated and compared; this may reveal further differences in thermal breakthrough behavior.

7

Conclusion

This thesis investigated the application of an unstructured approach to determine accurate well indices for exact well modeling. The established model was systematically verified and validated for synthetic and real models.

The unstructured well index calculation relies on a predefined number of structured reservoir blocks, typically including five blocks: one containing the well and 4 neighboring blocks in the horizontal plane. The model was generated accordingly to the number of blocks and simulated within open-DARTS for a short period of time to obtain reservoir pressure response and well flow rates. These parameters were used to calculate a new well index that would also allow for the exact well placements inside the block.

Model verification for a center well position showed that the well index obtained with an unstructured 5-block model remained close to that of the Peaceman approximation. A systematic validation study revealed that well index behavior is highly sensitive to well placement, local permeability contrasts, and the number of surrounding blocks considered in the model. The improved model performs significantly better when more reservoir blocks are considered, as evidenced by the enhanced accuracy of the 25-block and 9-block configurations over the 5-block approach for the two-dimensional synthetic reservoir. Incorporating more spatial information enables the model to better capture the well-reservoir interactions and approximate results from a full unstructured solution.

Spatial discretization methods within the finite volume framework of the open-DARTS reservoir simulator play a role in the accuracy of the attained results. The MPFA approximation yielded smoother results compared to the TPFA approach, because dissimilarities within the meshes caused different K-orthogonality errors for the TPFA discretizer. Nonetheless, TPFA discretization remained preferred due to acceptable errors and overall computational efficiency. Furthermore, the MPFA method can behave non-monotonic, which was deemed highly undesirable.

Application of the improved model to the GTD wells highlights its potential to offer more representative estimates than the Peaceman approach. Nevertheless, the current workflow could introduce over- and underestimations based on the extraction time value (the time needed to reach steady-state in the local model). This limitation can potentially be solved by incorporating adaptivity in time based on the criteria evaluating the convergence to the steady-state solution.

Furthermore, while the 9-block method was shown in the synthetic validation study to yield consistently higher well index values than the 5-block method, this trend is not observed in the Geothermie Delft (GTD) wells. For instance, in layers k = 33 and k = 34 of the DEL-GT-01 well. This discrepancy may stem from differences in reservoir heterogeneity amplitude in the GTD model compared to the synthetic validation case. Additionally, the possibility that the 9-block solutions had not yet fully converged at the extracted simulation times may partially explain the lower values. This suggests that further investigation is needed to identify the cause of this contradictory outcome. Lastly, although the improved well index model is computationally more demanding, it permits for more realistic well index modeling and reservoir simulation outcomes.

Well index results for the GTD reservoir yield lower amplitudes than the Peaceman approach. The impact of this amplitude change on the full reservoir simulation was tested by comparing simulation results for the 5-block, 9-block and Peaceman model. While production well temperature remained consistent across all models, differences arose in the pressure profiles of both the producer (DEL-GT-01) and injector (DEL-GT-02-S2) wells. The improved model captured more variations in the pressure profile, while the Peaceman model contains more steady profiles. This is likely due to the improved well model allowing for more exact and realistic well index modeling. Although production well temperature performance appeared similar, the shape and advance of the cold front were not evaluated and may reveal further differences in breakthrough behavior.

An important area for further research is the investigation into the effect of vertical permeability and vertical connectivity on well index estimations. While the improved well index model currently successfully accommodates lateral heterogeneity, it does not account for vertical permeability variations and vertical layer connectivity, limiting its accuracy for inclined wells such as those in the GTD project. Extending the model to three dimensions could further refine its predictive capabilities.

References

[1] Ivar Aavatsmark. “An Introduction to Multipoint Flux Approximations for Quadrilateral Grids”. In: *Computational Geosciences* 6 (Sept. 2002), pp. 405–432. DOI: 10.1023/A:1021291114475.

[2] Tarek Ahmed and D. Nathan Meehan. “Chapter 1 - Well Testing Analysis”. In: *Advanced Reservoir Management and Engineering (Second Edition)*. Ed. by Tarek Ahmed and D. Nathan Meehan. Second Edition. Boston: Gulf Professional Publishing, 2012, pp. 1–226. ISBN: 978-0-12-385548-0. DOI: https://doi.org/10.1016/B978-0-12-385548-0.00001-4. URL: https://www.sciencedirect.com/science/article/pii/B9780123855480000014.

[3] Kashy Aminian. “9 - Modeling and simulation for CBM production”. In: *Coal Bed Methane (Second Edition)*. Ed. by Pramod Thakur et al. Second Edition. Elsevier, 2020, pp. 169–174. ISBN: 978-0-12-815997-2. DOI: https://doi.org/10.1016/B978-0-12-815997-2.00009-3. URL: https://www.sciencedirect.com/science/article/pii/B9780128159972000093.

[4] Richard O. Baker, Harvey W. Yarranton, and Jerry L. Jensen. “3 - Basic Reservoir Engineering Calculations”. In: *Practical Reservoir Engineering and Characterization*. Ed. by Richard O. Baker, Harvey W. Yarranton, and Jerry L. Jensen. Boston: Gulf Professional Publishing, 2015, pp. 67–92. ISBN: 978-0-12-801811-8. DOI: https://doi.org/10.1016/B978-0-12-801811-8.00003-1. URL: https://www.sciencedirect.com/science/article/pii/B9780128018118000031.

[5] L. P. Dake. *Fundamentals of Reservoir Engineering*. Vol. 8. Developments in Petroleum Science. Elsevier, 1978. ISBN: 0-444-41830-X.

[6] Yu Ding, Gérard Renard, and Luce Weill. “Representation of Wells in Numerical Reservoir Simulation”. In: *SPE Reservoir Evaluation & Engineering* 1.01 (Feb. 1998), pp. 18–23. ISSN: 1094-6470. DOI: 10.2118/29123-PA. eprint: https://onepetro.org/REE/article-pdf/1/01/18/2592375/spe-29123-pa.pdf. URL: https://doi.org/10.2118/29123-PA.

[7] Ronald DiPippo. “Chapter 4 - Reservoir Engineering”. In: *Geothermal Power Plants*. Ed. by Ronald DiPippo. Oxford: Elsevier Science, 2005, pp. 53–83. ISBN: 978-1-85617-474-9. DOI: https://doi.org/10.1016/B978-185617474-9/50035-2. URL: https://www.sciencedirect.com/science/article/pii/B9781856174749500352.

[8] Rencheng Dong, Faruk O. Alpak, and Mary F. Wheeler. “Accurate Two-Phase Flow Simulation in Faulted Reservoirs by Combining Two-Point Flux Approximation and Mimetic Finite Difference Methods”. In: *SPE Journal* 28.01 (Feb. 2023), pp. 111–129. ISSN: 1086-055X. DOI: 10.2118/206298-PA. eprint: https://onepetro.org/SJ/article-pdf/28/01/111/3066700/spe-206298-pa.pdf. URL: https://doi.org/10.2118/206298-PA.

[9] EBN. *Infographic 2024 — ebn.nl*. https://www.ebn.nl/en/facts-figures/knowledge-base/infographic-2024/. [Accessed 07-01-2025]. 2024.

[10] *Geothermie Delft — geothermiedelft.nl*. https://geothermiedelft.nl/over-het-project. [Accessed 20-01-2025].

[11] H. González-García et al. “Financial performance analysis of the geothermal power station of Los Humeros, Mexico”. In: *Geothermics* 112 (2023), p. 102745. ISSN: 0375-6505. DOI: https://doi.org/10.1016/j.geothermics.2023.102745. URL: https://www.sciencedirect.com/science/article/pii/S0375650523000998.

[12] *History — tudelft.nl*. https://www.tudelft.nl/citg/over-faculteit/afdelingen/geoscience-engineering/research/geothermal/geothermal-science-and-engineering/research/campus-geothermal-project/history. [Accessed 20-01-2025].

[13] S. De Hoop, D. Voskov, and G. Bertotti. “Studying the Effects of Heterogeneity on Dissolution Processes Using Operator Based Linearization and High-Resolution LiDAR Data”. In: 2020.1 (2020), pp. 1–13. ISSN: 2214-4609. DOI: https://doi.org/10.3997/2214-4609.202035184. URL: https://www.earthdoc.org/content/papers/10.3997/2214-4609.202035184.

[14] J D Jansen et al. “The egg model - a geological ensemble for reservoir simulation”. en. In: *Geosci. Data J.* 1.2 (Nov. 2014), pp. 192–195.

[15] *Implementation and Application of a Hybrid Multipoint Flux Approximation for Reservoir Simulation on Corner-Point Grids*. Vol. SPE Annual Technical Conference and Exhibition. SPE Annual Technical Conference and Exhibition. Oct. 2005, SPE-95928–MS. DOI: 10.2118/95928-MS. eprint: https://onepetro.org/SPEATCE/proceedings-pdf/05ATCE/05ATCE/SPE-95928-MS/3848876/spe-95928-ms.pdf. URL: https://doi.org/10.2118/95928-MS.

[16] TNO - Adviesgroep Economische Zaken en Klimaat. *Annual Report 2023 - Natural resources and geothermal energy in the Netherlands | NLOG — nlog.nl*. https://www.nlog.nl/media/3298. [Accessed 20-01-2025]. Nov. 2024.

[17] Longlong Li et al. “Multiphase transient analysis for monitoring of CO2 flooding”. In: *Journal of Petroleum Science and Engineering* 160 (2018), pp. 537–554. DOI: 10.1016/j.petrol.2017.10.075.

[18] Reza Mohammadnia, Albert C. Reynolds, and Fahim Forouzanfar. “Monotonicity conditions for MPFA methods for a numerical well testing reservoir simulator”. In: *Journal of Petroleum Science and Engineering* 158 (2017), pp. 707–728. ISSN: 0920-4105. DOI: https://doi.org/10.1016/j.petrol.2017.08.047. URL: https://www.sciencedirect.com/science/article/pii/S0920410516305733.

[19] *Omvang en duurzaamheid - Geothermie Nederland — geothermie.nl*. https://geothermie.nl/geothermie/geothermie-omvang-en-duurzaamheid/. [Accessed 20-01-2025].

[20] Donald W. Peaceman. “Interpretation of Well-Block Pressures in Numerical Reservoir Simulation With Nonsquare Grid Blocks and Anisotropic Permeability”. In: *Society of Petroleum Engineers Journal* 23.03 (June 1983), pp. 531–543. ISSN: 0197-7520. DOI: 10.2118/10528-PA. eprint: https://onepetro.org/spejournal/article-pdf/23/03/531/2652459/spe-10528-pa.pdf. URL: https://doi.org/10.2118/10528-PA.

[21] Donald W. Peaceman. “Interpretation of Well-Block Pressures in Numerical Reservoir Simulation(includes associated paper 6988)”. In: *Society of Petroleum Engineers Journal* 18 (1978), pp. 183–194. URL: https://api.semanticscholar.org/CorpusID:93348663.

[22] Donald W. Peaceman. “Interpretation of Wellblock Pressures in Numerical Reservoir Simulations Part 3—Off-Center and Multiple Wells Within a Wellblock”. In: *SPE Reservoir Engineering* 5.02 (May 1990), pp. 227–232. ISSN: 0885-9248. DOI: 10.2118/16976-PA. eprint: https://onepetro.org/RE/article-pdf/5/02/227/2624416/spe-16976-pa.pdf. URL: https://doi.org/10.2118/16976-PA.

[23] X. Raynaud et al. “Toward Accurate Reservoir Simulations on Unstructured Grids: Design of Simple Error Estimators and Critical Benchmarking of Consistent Discretization Methods for Practical Implementation”. In: *SPE Journal* 26.06 (Dec. 2021), pp. 4109–4127. ISSN: 1086-055X. DOI: 10.2118/203920-PA. eprint: https://onepetro.org/SJ/article-pdf/26/06/4109/2553513/spe-203920-pa.pdf. URL: https://doi.org/10.2118/203920-PA.

[24] *A Generalized Finite Volume Discretization Method for Reservoir Simulation*. Vol. SPE Symposium on Reservoir Simulation. SPE Reservoir Simulation Conference. Feb. 1989, SPE-18414–MS. DOI: 10.2118/18414-MS. eprint: https://onepetro.org/spersc/proceedings-pdf/89RS/89RS/SPE-18414-MS/3216216/spe-18414-ms.pdf. URL: https://doi.org/10.2118/18414-MS.

[25] Jones Shu. *Comparison of Various Techniques for Computing Well Index*. Available at: https://purl.stanford.edu/xk906gg6034. 2005. URL: https://purl.stanford.edu/xk906gg6034.

[26] Ho-Jeen Su. “Modeling Off-Center Wells in Reservoir Simulation”. In: *SPE Reservoir Engineering* 10.01 (Feb. 1995), pp. 47–51. ISSN: 0885-9248. DOI: 10.2118/25275-PA. eprint: https://onepetro.org/RE/article-pdf/10/01/47/2602718/spe-25275-pa.pdf. URL: https://doi.org/10.2118/25275-PA.

[27] Cenk Temizel et al. “Chapter 4 - Production engineering formulas and calculations”. In: *Formulas and Calculations for Petroleum Engineering*. Ed. by Cenk Temizel et al. Gulf Professional Publishing, 2019, pp. 203–256. ISBN: 978-0-12-816508-9. DOI: https://doi.org/10.1016/B978-0-12-816508-9.00004-4. URL: https://www.sciencedirect.com/science/article/pii/B9780128165089000044.

[28] P. J. Vardon et al. “A Research and Energy Production Geothermal Project on the TU Delft Campus: Project Implementation and Initial Data Collection”. In: *Proceedings of the 49th Workshop on Geothermal Reservoir Engineering*. Stanford University, 2024. URL: https://pangea.stanford.edu/ERE/db/GeoConf/papers/SGW/2024/Vardon.pdf.

[29] Denis Voskov et al. “open Delft Advanced Research Terra Simulator (open-DARTS)”. In: *Journal of Open Source Software* 9.99 (2024), p. 6737. DOI: 10.21105/joss.06737. URL: https://doi.org/10.21105/joss.06737.

[30] MAW Vrijlandt et al. “ThermoGIS update: a renewed view on geothermal potential in the Netherlands”. In.

[31] Cees J.L. Willems et al. “Geology of the Upper Jurassic to Lower Cretaceous geothermal aquifers in the West Netherlands Basin – an overview”. In: *Netherlands Journal of Geosciences* 99 (2020), e1. DOI: 10.1017/njg.2020.1.

[32] Alina Yapparova et al. “A Peaceman-type well model for the 3D Control Volume Finite Element Method and numerical simulations of supercritical geothermal resource utilization”. In: *Geothermics* 105 (2022), p. 102516. ISSN: 0375-6505. DOI: https://doi.org/10.1016/j.geothermics.2022.102516. URL: https://www.sciencedirect.com/science/article/pii/S0375650522001614.

[33] Zhao Zhang et al. “Numerical simulation of skin factors for perforated wells with crushed zone and drilling-fluid damage in tight gas reservoirs”. In: *Journal of Natural Gas Science and Engineering* 90 (2021), p. 103907. ISSN: 1875-5100. DOI: https://doi.org/10.1016/j.jngse.2021.103907. URL: https://www.sciencedirect.com/science/article/pii/S1875510021001141.

A

Repository framework

A.1. Overview

The repository contains the source code and models utilized for this study. It holds the codes implemented to generate unstructured meshes, run the improved well index model, read the CPG reservoir model and find intersections. The models are hosted on GitLab: `gitlab.com/agodschalk00/thesis-annique-godschalk`.

A.1.1. Directory Structure

The repository is structured in the following manner;

```
thesis-annique-godschalk/
   Full unstructured/
       main_geothermal.py
       model_geothermal.py
       unstruct_reservoir.py
   GTD_application/
       GTD_intersections/
|    |      intersections_DEL-GT-01.txt
|    |      intersections_DEL-GT-02-S2.txt
|       cpg_model.py
|       cpg_reservoir.py
|       main_geothermal_GTD.py
|       model_geothermal_GTD.py
|       unstruct_reservoir.py
   Local model/
       Simple_model_well_placement.txt
       main_geothermal_local.py
       model_geothermal_local.py
       unstruct_reservoir.py
   MPFA/
       Full unstructured/
|    |      model_mpfa.py
|    |      reservoir_mpfa.py
       Local model/
|    |      model_mpfa_local.py
|    |      reservoir_mpfa_local.py
       main_mpfa.py
   Meshes/
       5block_mesh.py
       9block_mesh.py
```

```
fullunstructured_map_mesh.py
mesh_GTD.py
```

A.2. File Descriptions

This section contains the summary of the key files and directories included in the repository:

- `Full unstructured/`: This map contains the .py files used to compute well index values based on the full unstructured reservoir grid for the two-dimensional synthetic reservoir. The spatial discretization within the finite volume framework is performed using a two-point flux approximation, discretization of the mesh is performed in `unstruct_reservoir.py`. Furthermore, `model_geothermal.py` assigns permeability values to the unstructured mesh based on the predefined permeability realization.
- `GTD_application/`: The map contains all models and files utilized to apply the improved well model to the Geothermie Delft (GTD) project wells.
  - `GTD_intersections/`: The following map contains the computed intersections for both the DEL-GT-01 and DEL-GT-02-S2 well. The text files contain intersection points, the block index of the block the intersection corresponds to (i,j,k) and the face center of the face that the well intersects.
  - `cpg_model.py` & `cpg_reservoir.py`: These files are used to read the CPG format of the GTD reservoir model and determine intersection accordingly to the faces of the reservoir model. For this `face_nodepos`, `face_nodes`, `node_coordinates` and `face_cells` are needed.
  - Remaining files: The remainder of the files in this directory (e.g. `main_geothermal_GTD.py`, `model_geothermal_GTD.py` and `unstruct_reservoir.py`) are employed to find well indices for the GTD wells. Discretization is again done by a two-point flux approximation within `unstruct_reservoir.py`. The `model_geothermal_GTD.py` code can be altered to accept both the 5-block or 9-block model.
- `Local model/`: The directory contains models for determining well indices based on the specified number of blocks within the model, either 5, 9 or 25. Two-point flux approximation is utilized. Additionally, well placement can either be specified within the model or by a text file. An example of such a text file is `Simple_model_well_placement.txt`.
- `MPFA/`: Folder containing the models for well index determination based on the full unstructured approach and the local approach of either 5, 9 or 25 blocks. The file `main_mpfa.py` was altered to fit either the full unstructured or the local model. Correct permeability profiles of the blocks were again assigned within `model_mpfa.py` and `model_mpfa_local.py`.
- `Meshes/`: Directory containing all necessary files to generate meshes corresponding to the above mentioned models.
  - `5block_mesh.py` & `9block_mesh.py`: Files contain mesh generation for the local models of 5 and 9 blocks. Code was extended similarly for the 25 block model.
  - `fullunstructured_map_mesh.py` contains an improved code from the previous mesh files that allows for unstructured mesh generation of the two-dimensional synthetic reservoir.
  - `mesh_GTD.py`: Code file for the mesh generation based on the extracted intersections, the code itself is similar to `5block_mesh.py` and `9block_mesh.py`. Nonetheless, this code also contains reading the intersection text files and determining the correct well placement in the two-dimensional plane.

B

Additional Figures

B.1. Improved Model Verification

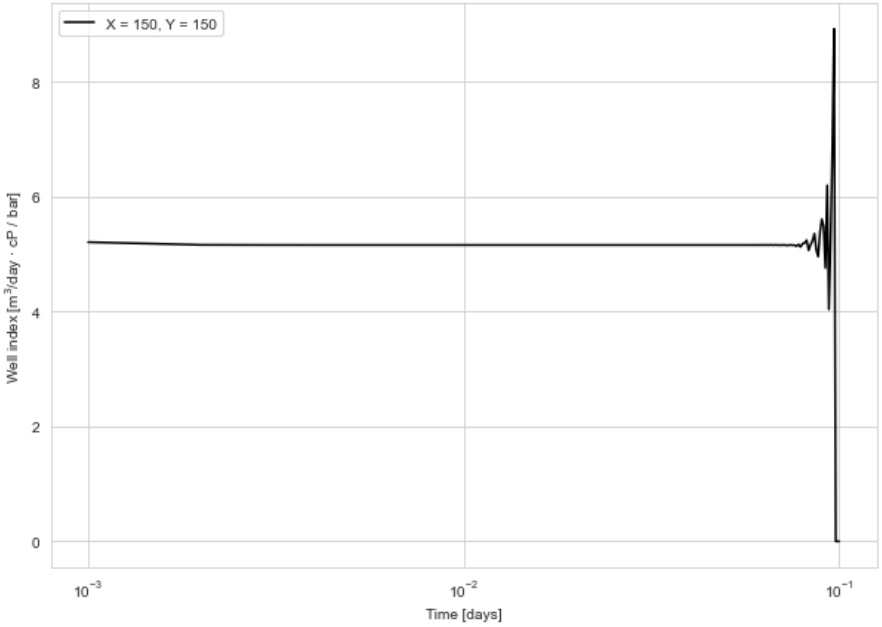

Figure B.1: The improved well index model for a center position at position (150, 150). Depletion for the model is reached around 0.10 days for a permeability of 50 mD, the solution will first deviate before turning to 0.

B.2. Validation study

Validation study: Meshes

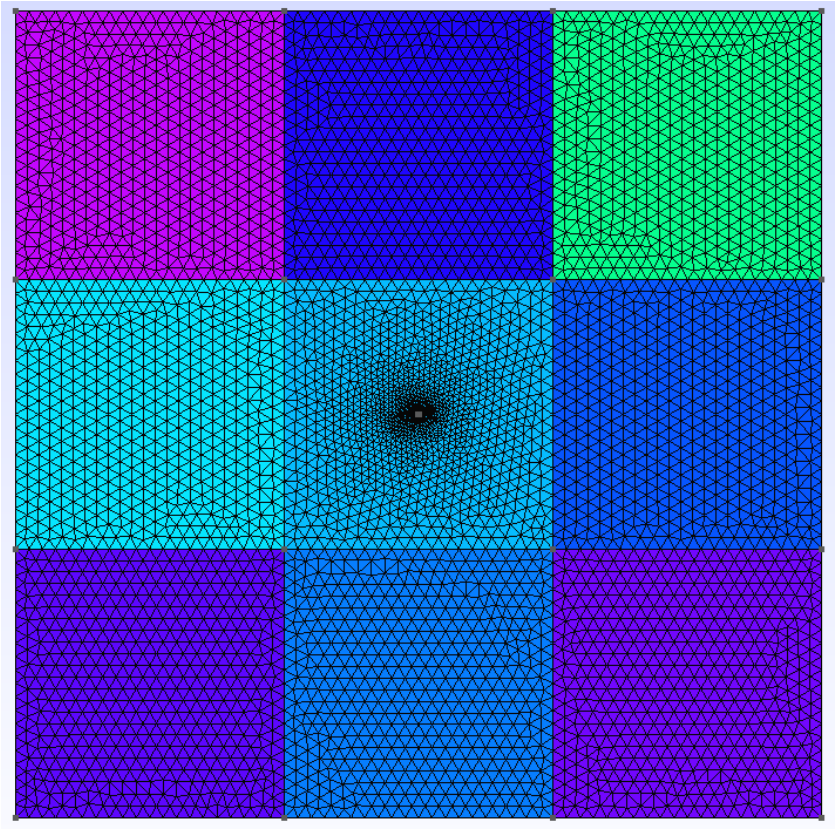

Figure B.2: The obtained mesh for the 9-block case with well placement at location 150, 150.

Validation study: TPFA Results

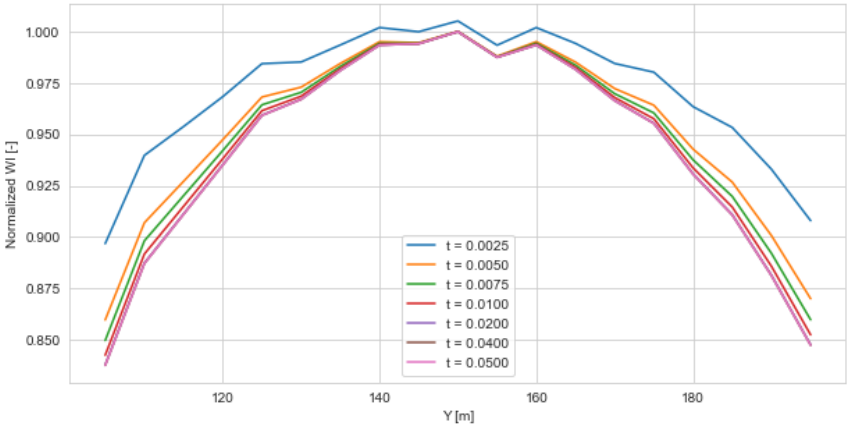

Figure B.3: Well index as a function of the position along the y-axis at different times.

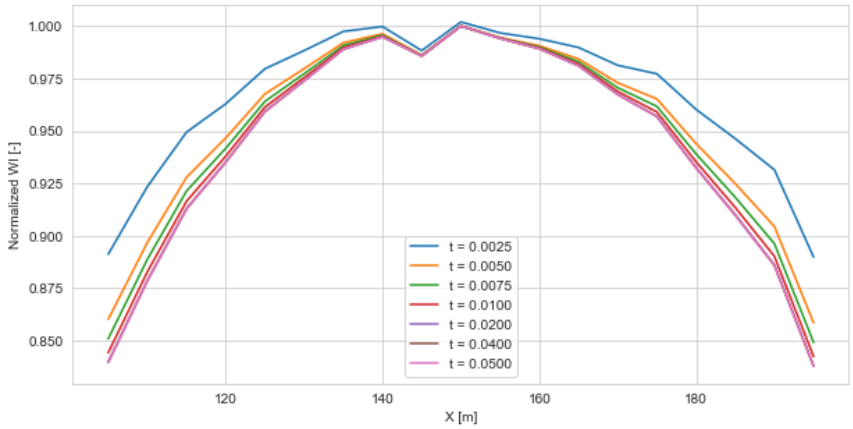

Figure B.4: Well index as a function of the position along the x-axis at different times.

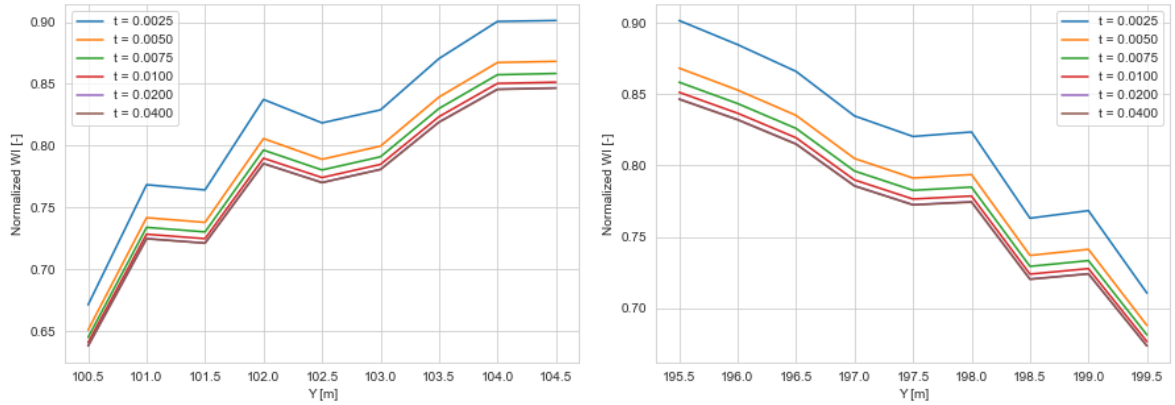

(a) Bottom edge.

(b) Top edge.

Figure B.5: Well transmissibility results for the bottom (a) and top edge (b) of the vertical axis plotted against well position for different times.

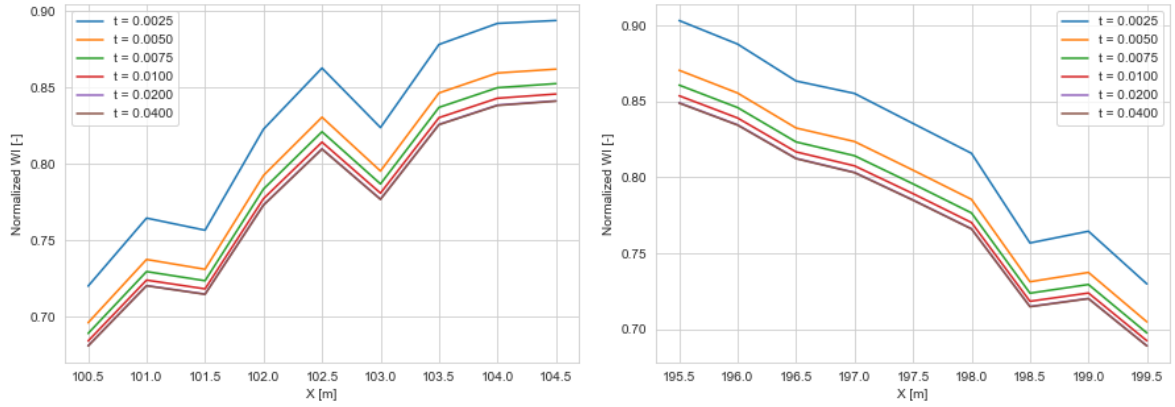

(a) Left edge.

(b) Right edge.

Figure B.6: Well transmissibility results for the left (a) and right edge (b) of the horizontal axis plotted against well position for different times.

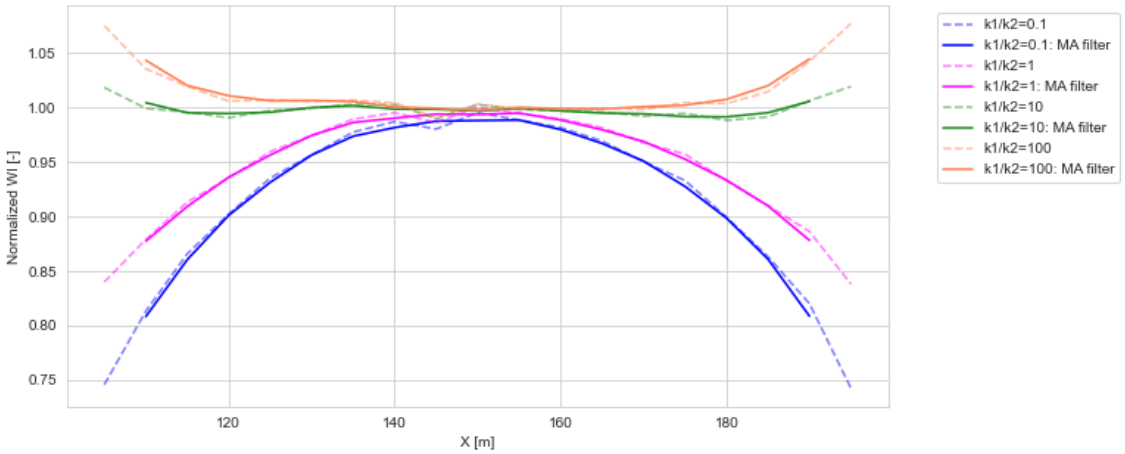

Figure B.7: Well index as a function of well position x at time t = 0.04 days using different permeability relationship. Both unfiltered and filtered results are displayed, using a dashed and solid line respectively.

Validation study: Synthetic reservoir model

MPFA results

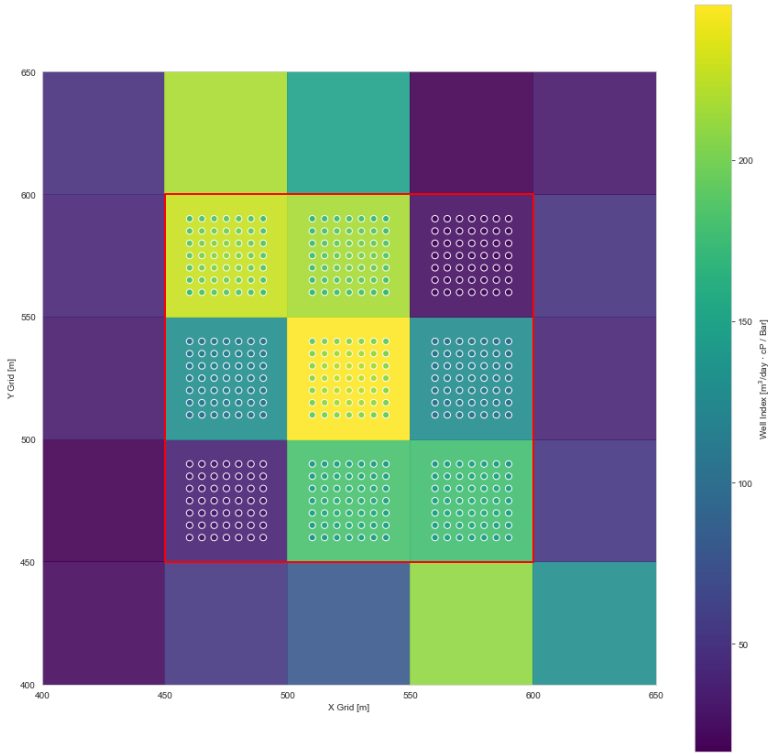

Figure B.8: Well index map obtained using the 5-block approach and MPFA discretization of the mesh.

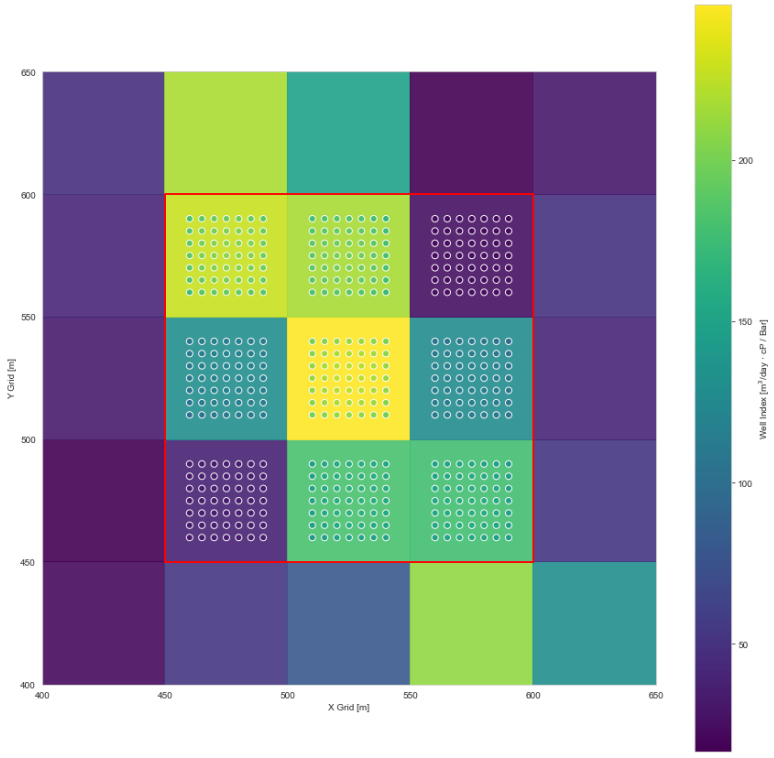

Figure B.9: Well index map obtained using the 9-block approach and MPFA discretization of the mesh.

B.3. Geothermie Delft (GTD) model

Well trajectory intersections

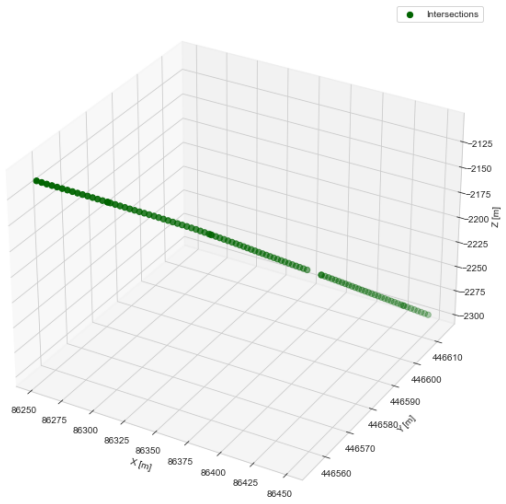

Figure B.10: Obtained well intersections between the well and the reservoir cells.

#	Intersection			Cell Index			Face Center		
	x	y	z	i	j	k	x_c	y_c	z_c
1	86252.28	446554.96	2110.54	61	61	1	86260.16	446572.11	2115.53
2	86254.64	446555.68	2112.67	61	61	2	86260.16	446572.12	2117.03
3	86257.00	446556.40	2114.81	61	61	3	86260.16	446572.12	2118.53
4	86259.36	446557.17	2116.94	61	61	4	86260.16	446572.12	2120.03
5	86261.71	446557.93	2119.08	61	61	5	86260.16	446572.12	2121.53
6	86264.06	446558.69	2121.21	61	61	6	86260.16	446572.12	2123.03
7	86266.40	446559.46	2123.33	61	61	7	86260.16	446572.12	2124.54
8	86268.73	446560.21	2125.46	61	61	8	86260.16	446572.12	2126.04
9	86271.06	446560.96	2127.57	61	61	9	86260.16	446572.12	2127.54
10	86273.39	446561.71	2129.69	61	61	10	86260.16	446572.12	2129.04
11	86275.71	446562.45	2131.80	61	61	11	86260.16	446572.12	2130.54
12	86278.03	446563.19	2133.91	61	61	12	86260.16	446572.12	2132.04
13	86280.35	446563.93	2136.02	61	61	13	86260.16	446572.12	2133.54
14	86282.68	446564.66	2138.12	61	61	14	86260.17	446572.12	2135.04
15	86284.99	446565.39	2140.23	61	61	15	86260.17	446572.12	2136.55
16	86285.09	446565.42	2140.31	62	61	15	86285.09	446572.19	2142.31
17	86286.37	446565.82	2141.47	62	61	16	86309.99	446572.10	2147.66
18	86288.65	446566.54	2143.54	62	61	17	86309.99	446572.10	2149.14
19	86290.93	446567.26	2145.61	62	61	18	86309.99	446572.10	2150.62
20	86293.20	446567.98	2147.67	62	61	19	86309.99	446572.10	2152.10
21	86295.48	446568.70	2149.73	62	61	20	86309.99	446572.10	2153.59
22	86297.76	446569.42	2151.79	62	61	21	86309.99	446572.10	2155.07
23	86300.07	446570.16	2153.86	62	61	22	86309.99	446572.10	2156.55
24	86302.37	446570.89	2155.92	62	61	23	86309.99	446572.10	2158.03
25	86304.66	446571.62	2157.98	62	61	24	86309.99	446572.10	2159.51
26	86306.96	446572.34	2160.04	62	61	25	86309.99	446572.10	2160.99
27	86309.26	446573.04	2162.09	62	61	26	86309.99	446572.10	2162.47
28	86311.56	446573.73	2164.14	62	61	27	86309.99	446572.10	2163.95
29	86313.86	446574.42	2166.18	62	61	28	86309.99	446572.10	2165.43
30	86316.16	446575.11	2168.23	62	61	29	86309.99	446572.10	2166.91

#	Intersection			Cell Index			Face Center		
	x	y	z	i	j	k	x_c	y_c	z_c
31	86318.45	446575.80	2170.27	62	61	30	86309.99	446572.10	2168.40
32	86320.74	446576.49	2172.30	62	61	31	86309.99	446572.10	2169.88
33	86323.03	446577.17	2174.34	62	61	32	86309.99	446572.10	2171.36
34	86325.31	446577.86	2176.37	62	61	33	86309.99	446572.10	2172.84
35	86327.57	446578.53	2178.39	62	61	34	86309.99	446572.10	2174.32
36	86329.74	446579.15	2180.39	62	61	35	86309.99	446572.10	2175.80
37	86331.92	446579.76	2182.38	62	61	36	86309.99	446572.10	2177.28
38	86334.09	446580.37	2184.37	62	61	37	86309.99	446572.10	2178.76
39	86334.93	446580.61	2185.15	63	61	37	86334.93	446572.21	2183.84
40	86335.52	446580.78	2185.69	63	61	38	86359.84	446572.11	2188.57
41	86337.59	446581.37	2187.59	63	61	39	86359.84	446572.11	2190.02
42	86339.66	446581.95	2189.49	63	61	40	86359.84	446572.11	2191.47
43	86341.73	446582.54	2191.39	63	61	41	86359.84	446572.11	2192.92
44	86343.80	446583.13	2193.28	63	61	42	86359.84	446572.11	2194.37
45	86345.86	446583.71	2195.18	63	61	43	86359.84	446572.11	2195.82
46	86347.89	446584.28	2197.06	63	61	44	86359.84	446572.11	2197.27
48	86349.84	446584.83	2198.93	63	61	45	86359.84	446572.11	2198.73
49	86351.80	446585.38	2200.79	63	61	46	86359.84	446572.11	2200.18
50	86353.76	446585.92	2202.66	63	61	47	86359.84	446572.11	2201.63
51	86355.71	446586.47	2204.52	63	61	48	86359.84	446572.11	2203.08
52	86357.65	446587.02	2206.38	63	61	49	86359.84	446572.11	2204.52
53	86359.58	446587.58	2208.23	63	61	50	86359.84	446572.11	2205.98
54	86361.51	446588.14	2210.09	63	61	51	86359.84	446572.11	2207.43
55	86363.44	446588.70	2211.94	63	61	52	86359.84	446572.11	2208.88
56	86365.37	446589.25	2213.79	63	61	53	86359.84	446572.11	2210.33
57	86367.29	446589.81	2215.64	63	61	54	86359.84	446572.11	2211.78
58	86369.20	446590.37	2217.49	63	61	55	86359.84	446572.11	2213.23
59	86371.12	446590.92	2219.33	63	61	56	86359.84	446572.11	2214.68
60	86373.03	446591.48	2221.17	63	61	57	86359.84	446572.11	2216.13
61	86374.94	446592.04	2223.01	63	61	58	86359.84	446572.11	2217.58
62	86376.84	446592.59	2224.85	63	61	59	86359.84	446572.11	2219.04
63	86378.74	446593.16	2226.69	63	61	60	86359.84	446572.11	2220.49
64	86380.64	446593.72	2228.53	63	61	61	86359.84	446572.11	2221.94
65	86382.54	446594.29	2230.36	63	61	62	86359.84	446572.11	2223.39
66	86384.43	446594.85	2232.19	63	61	63	86359.84	446572.11	2224.84
67	86391.68	446597.04	2239.26	64	62	66	86409.66	446597.04	2241.28
68	86391.83	446597.09	2239.41	64	62	67	86409.66	446621.94	2245.71
69	86393.64	446597.64	2241.18	64	62	68	86409.66	446621.94	2247.16
70	86395.44	446598.19	2242.95	64	62	69	86409.66	446621.94	2248.61
71	86397.21	446598.72	2244.70	64	62	70	86409.66	446621.94	2250.05
72	86398.96	446599.25	2246.46	64	62	71	86409.66	446621.94	2251.50
73	86400.71	446599.78	2248.21	64	62	72	86409.66	446621.94	2252.95
74	86402.45	446600.30	2249.96	64	62	73	86409.66	446621.94	2254.40
75	86404.20	446600.83	2251.72	64	62	74	86409.66	446621.94	2255.84
76	86405.94	446601.35	2253.47	64	62	75	86409.66	446621.94	2257.29
77	86407.65	446601.87	2255.21	64	62	76	86409.66	446621.94	2258.74
78	86409.37	446602.39	2256.95	64	62	77	86409.66	446621.94	2260.19
79	86411.08	446602.92	2258.70	64	62	78	86409.66	446621.94	2261.63
80	86412.79	446603.44	2260.44	64	62	79	86409.66	446621.94	2263.08
81	86414.50	446603.96	2262.18	64	62	80	86409.66	446621.94	2264.53
82	86416.22	446604.48	2263.92	64	62	81	86409.66	446621.94	2265.97
83	86417.93	446605.00	2265.66	64	62	82	86409.65	446621.94	2267.42
84	86419.65	446605.52	2267.40	64	62	83	86409.65	446621.94	2268.87

#	Intersection			Cell Index			Face Center		
	x	y	z	i	j	k	x_c	y_c	z_c
85	86421.36	446606.03	2269.14	64	62	84	86409.65	446621.94	2270.32
86	86423.07	446606.55	2270.88	64	62	85	86409.65	446621.94	2271.76
87	86424.78	446607.07	2272.61	64	62	86	86409.65	446621.94	2273.21
88	86426.50	446607.59	2274.35	64	62	87	86409.65	446621.94	2274.66
89	86428.21	446608.11	2276.08	64	62	88	86409.65	446621.94	2276.11
90	86429.92	446608.63	2277.82	64	62	89	86409.65	446621.94	2277.55
91	86431.62	446609.14	2279.55	64	62	90	86409.65	446621.94	2279.00
92	86433.33	446609.66	2281.28	64	62	91	86409.65	446621.94	2280.45
93	86434.62	446610.05	2282.58	65	62	91	86434.62	446621.98	2283.70
94	86435.06	446610.18	2283.02	65	62	93	86459.51	446621.89	2290.06
95	86436.88	446610.73	2284.86	65	62	94	86459.51	446621.89	2291.49
96	86438.71	446611.27	2286.69	65	62	95	86459.51	446621.89	2292.92
97	86440.54	446611.82	2288.53	65	62	96	86459.51	446621.89	2294.34
98	86442.37	446612.37	2290.37	65	62	97	86459.51	446621.89	2295.79
99	86444.21	446612.92	2292.21	65	62	98	86459.51	446621.89	2297.22
100	86446.08	446613.48	2294.06	65	62	99	86459.51	446621.89	2298.66
101	86447.95	446614.04	2295.92	65	62	100	86459.51	446621.89	2300.09

Table B.1: Well–Reservoir Intersection Points and Corresponding Grid Blocks for the DEL-GT-01 well.

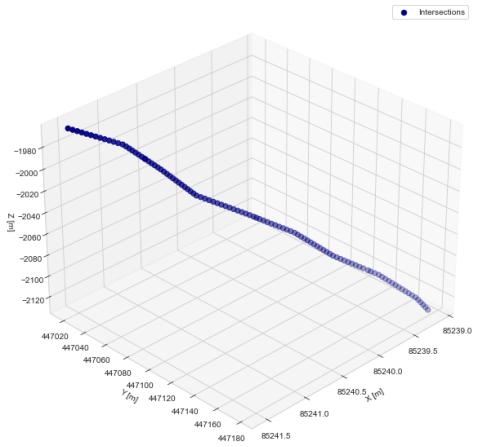

Figure B.11: Well intersections between the DEL-GT-02-S2 well and the reservoir model.

#	Intersection			Cell Index			Face Center		
	x	y	z	i	j	k	x_c	y_c	z_c
1	85241.53	447018.86	1962.82	41	70	1	85263.29	447020.71	1967.71
2	85241.49	447020.25	1964.58	41	70	2	85263.29	447020.71	1969.18
3	85241.45	447021.62	1966.34	41	70	3	85263.29	447020.71	1970.65
4	85241.41	447023.00	1968.09	41	70	4	85263.29	447020.71	1972.12
5	85241.38	447024.37	1969.84	41	70	5	85263.29	447020.71	1973.60
6	85241.34	447025.75	1971.59	41	70	6	85263.29	447020.71	1975.07
7	85241.30	447027.11	1973.33	41	70	7	85263.29	447020.71	1976.54
8	85241.26	447028.48	1975.07	41	70	8	85263.29	447020.71	1978.01
9	85241.23	447029.84	1976.81	41	70	9	85263.29	447020.71	1979.49
10	85241.19	447031.21	1978.55	41	70	10	85263.29	447020.71	1980.96
11	85241.15	447032.56	1980.28	41	70	11	85263.29	447020.71	1982.43

#	Intersection			Cell Index			Face Center		
	x	y	z	i	j	k	x_c	y_c	z_c
12	85241.11	447033.92	1982.01	41	70	12	85263.29	447020.71	1983.90
13	85241.07	447035.27	1983.73	41	70	13	85263.29	447020.71	1985.38
14	85241.05	447036.76	1985.49	41	70	14	85263.29	447020.71	1986.85
15	85241.04	447038.28	1987.25	41	70	15	85263.29	447020.71	1988.32
16	85241.02	447039.80	1989.00	41	70	16	85263.29	447020.71	1989.79
17	85241.00	447041.31	1990.75	41	70	17	85263.29	447020.71	1991.27
18	85240.98	447042.82	1992.50	41	70	18	85263.29	447020.71	1992.74
19	85240.96	447044.33	1994.25	41	70	19	85263.29	447020.71	1994.21
20	85240.95	447045.64	1995.77	41	71	19	85263.36	447045.64	2000.07
21	85240.94	447046.09	1996.28	41	71	20	85263.28	447070.55	2006.09
22	85240.92	447047.59	1998.02	41	71	21	85263.28	447070.55	2007.51
23	85240.91	447049.09	1999.76	41	71	22	85263.28	447070.55	2008.93
24	85240.89	447050.58	2001.49	41	71	23	85263.28	447070.55	2010.34
25	85240.87	447052.07	2003.21	41	71	24	85263.28	447070.55	2011.76
26	85240.85	447053.56	2004.94	41	71	25	85263.28	447070.55	2013.17
27	85240.83	447055.16	2006.68	41	71	26	85263.28	447070.55	2014.59
28	85240.82	447056.77	2008.41	41	71	27	85263.28	447070.55	2016.01
29	85240.80	447058.37	2010.15	41	71	28	85263.28	447070.55	2017.42
30	85240.79	447059.96	2011.87	41	71	29	85263.28	447070.55	2018.84
31	85240.77	447061.55	2013.60	41	71	30	85263.28	447070.55	2020.25
32	85240.76	447063.14	2015.31	41	71	31	85263.28	447070.55	2021.67
33	85240.74	447064.72	2017.02	41	71	32	85263.28	447070.55	2023.08
34	85240.73	447066.30	2018.73	41	71	33	85263.28	447070.55	2024.50
35	85240.71	447067.87	2020.43	41	71	34	85263.28	447070.55	2025.92
36	85240.70	447069.44	2022.13	41	71	35	85263.28	447070.55	2027.33
37	85240.68	447071.00	2023.82	41	71	36	85263.28	447070.55	2028.75
38	85240.67	447072.56	2025.51	41	71	37	85263.28	447070.55	2030.16
39	85240.64	447074.14	2027.19	41	71	38	85263.28	447070.55	2031.58
40	85240.60	447075.72	2028.87	41	71	39	85263.28	447070.55	2032.99
41	85240.57	447077.30	2030.55	41	71	40	85263.28	447070.55	2034.41
42	85240.54	447078.87	2032.22	41	71	41	85263.28	447070.55	2035.83
43	85240.51	447080.44	2033.88	41	71	42	85263.28	447070.55	2037.24
44	85240.48	447082.00	2035.54	41	71	43	85263.28	447070.55	2038.66
45	85240.45	447083.55	2037.20	41	71	44	85263.28	447070.55	2040.07
46	85240.42	447085.11	2038.85	41	71	45	85263.28	447070.55	2041.49
47	85240.39	447086.65	2040.49	41	71	46	85263.28	447070.55	2042.91
48	85240.35	447088.20	2042.13	41	71	47	85263.28	447070.55	2044.32
49	85240.32	447089.74	2043.77	41	71	48	85263.28	447070.55	2045.74
50	85240.29	447091.27	2045.40	41	71	49	85263.28	447070.55	2047.15
51	85240.26	447092.81	2047.02	41	71	50	85263.28	447070.55	2048.57
52	85240.23	447094.35	2048.65	41	71	51	85263.28	447070.55	2049.98
53	85240.21	447095.48	2049.85	41	72	51	85263.37	447095.48	2055.01
54	85240.19	447096.71	2051.14	41	72	52	85263.28	447120.39	2060.60
55	85240.16	447098.28	2052.80	41	72	53	85263.28	447120.39	2061.96
56	85240.13	447099.84	2054.46	41	72	54	85263.28	447120.39	2063.32
57	85240.10	447101.41	2056.11	41	72	55	85263.28	447120.39	2064.69
58	85240.07	447102.97	2057.76	41	72	56	85263.28	447120.39	2066.05
59	85240.04	447104.52	2059.40	41	72	57	85263.28	447120.39	2067.41
60	85240.01	447106.08	2061.04	41	72	58	85263.28	447120.39	2068.78
61	85239.99	447107.63	2062.68	41	72	59	85263.28	447120.40	2070.14
62	85239.96	447109.17	2064.32	41	72	60	85263.28	447120.39	2071.50
63	85239.93	447110.73	2065.95	41	72	61	85263.28	447120.39	2072.87
64	85239.91	447112.36	2067.59	41	72	62	85263.28	447120.39	2074.23

#	Intersection			Cell Index			Face Center		
	x	y	z	i	j	k	x_c	y_c	z_c
65	85239.89	447114.00	2069.24	41	72	63	85263.28	447120.39	2075.59
66	85239.87	447115.63	2070.88	41	72	64	85263.28	447120.39	2076.96
67	85239.85	447117.25	2072.51	41	72	65	85263.28	447120.39	2078.32
68	85239.83	447118.87	2074.14	41	72	66	85263.28	447120.38	2079.68
69	85239.81	447120.49	2075.77	41	72	67	85263.27	447120.39	2081.05
70	85239.79	447122.11	2077.39	41	72	68	85263.27	447120.39	2082.41
71	85239.77	447123.72	2079.01	41	72	69	85263.27	447120.39	2083.77
72	85239.76	447125.33	2080.63	41	72	70	85263.27	447120.39	2085.14
73	85239.74	447126.93	2082.24	41	72	71	85263.27	447120.39	2086.50
74	85239.72	447128.53	2083.85	41	72	72	85263.27	447120.39	2087.86
75	85239.70	447130.13	2085.46	41	72	73	85263.27	447120.39	2089.23
76	85239.67	447131.79	2087.07	41	72	74	85263.27	447120.39	2090.59
77	85239.64	447133.44	2088.68	41	72	75	85263.27	447120.39	2091.95
78	85239.62	447135.09	2090.28	41	72	76	85263.27	447120.39	2093.32
79	85239.59	447136.73	2091.88	41	72	77	85263.27	447120.39	2094.68
80	85239.56	447138.37	2093.47	41	72	78	85263.27	447120.38	2096.04
81	85239.54	447140.01	2095.07	41	72	79	85263.27	447120.38	2097.41
82	85239.51	447141.64	2096.66	41	72	80	85263.27	447120.38	2098.77
83	85239.48	447143.27	2098.24	41	72	81	85263.27	447120.38	2100.13
84	85239.45	447145.33	2100.24	41	73	81	85263.33	447145.33	2105.16
85	85239.43	447146.53	2101.40	41	73	82	85263.27	447170.23	2111.60
86	85239.40	447148.30	2103.13	41	73	83	85263.27	447170.23	2112.95
87	85239.37	447150.07	2104.85	41	73	84	85263.27	447170.23	2114.31
88	85239.35	447151.82	2106.57	41	73	85	85263.27	447170.23	2115.66
89	85239.33	447153.57	2108.30	41	73	86	85263.27	447170.23	2117.01
90	85239.31	447155.32	2110.02	41	73	87	85263.27	447170.23	2118.36
91	85239.29	447157.07	2111.74	41	73	88	85263.27	447170.23	2119.71
92	85239.27	447158.83	2113.47	41	73	89	85263.27	447170.23	2121.06
93	85239.25	447160.58	2115.20	41	73	90	85263.27	447170.23	2122.42
94	85239.23	447162.34	2116.92	41	73	91	85263.27	447170.23	2123.77
95	85239.21	447164.09	2118.65	41	73	92	85263.27	447170.23	2125.12
96	85239.19	447165.85	2120.38	41	73	93	85263.27	447170.23	2126.47
97	85239.17	447167.61	2122.11	41	73	94	85263.27	447170.23	2127.82
98	85239.15	447169.36	2123.84	41	73	95	85263.27	447170.23	2129.17
99	85239.14	447171.11	2125.57	41	73	96	85263.27	447170.23	2130.52
100	85239.14	447172.84	2127.30	41	73	97	85263.27	447170.23	2131.88
101	85239.13	447174.58	2129.03	41	73	98	85263.27	447170.23	2133.23
102	85239.12	447176.32	2130.76	41	73	99	85263.27	447170.23	2134.58
103	85239.12	447178.06	2132.50	41	73	100	85263.26	447170.23	2135.93

Table B.2: Well–Reservoir Intersection Points and Corresponding Grid Blocks for the DEL-GT-012-S2 well.

Well index solutions

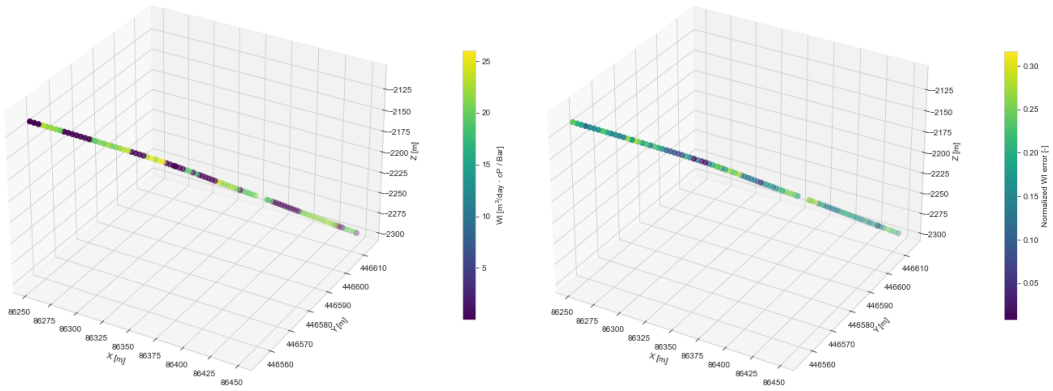

(a) WI solution **(b)** Normalized WI error

Figure B.12: Well index results using a 5-block unstructured approach for the DEL-GT-01 well. The full solution (a) and a normalized error (b) using the Peaceman well index are presented.

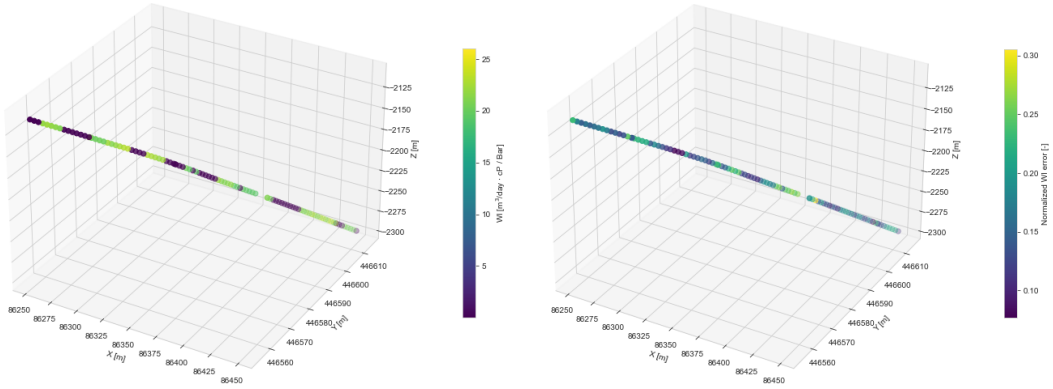

(a) WI solution **(b)** Normalized WI error

Figure B.13: Well index results using a 9-block unstructured approach for the DEL-GT-01 well. The full solution (a) and a normalized error (b) using the Peaceman well index are presented.

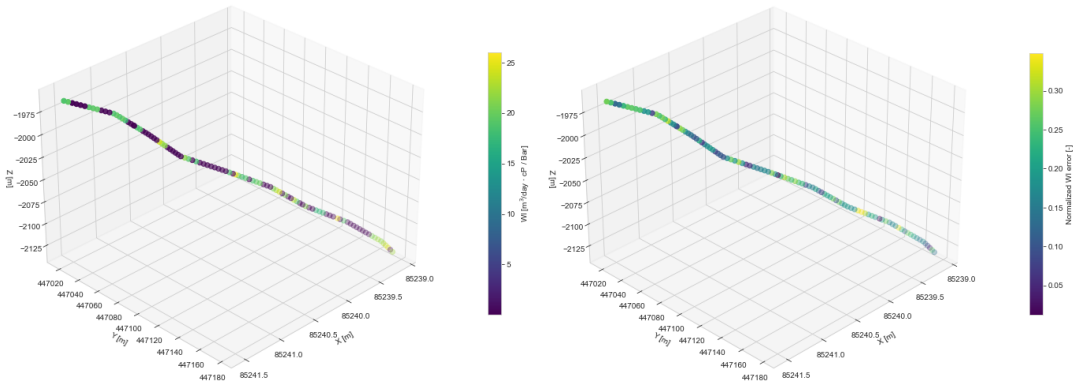

(a) WI solution **(b)** Normalized WI error

Figure B.14: Well index results using a 5-block unstructured approach for the DEL-GT-02-S2 well. The full solution (a) and a normalized error (b) using the Peaceman well index are shown.

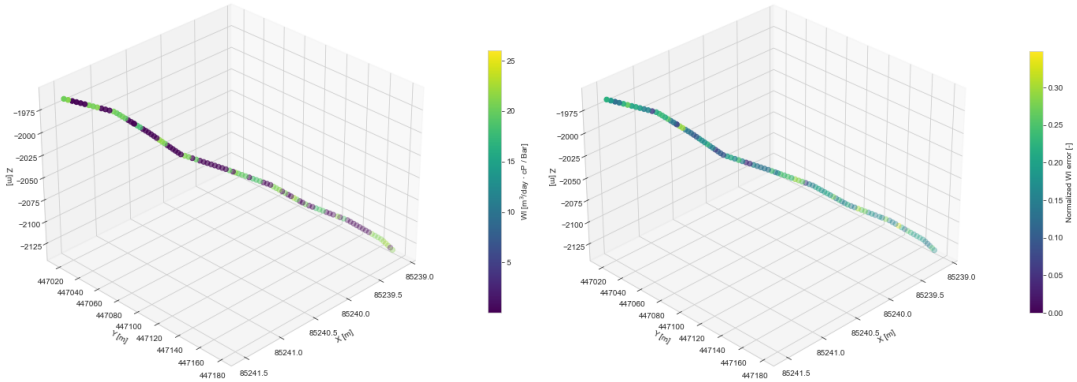

(a) WI solution **(b)** Normalized WI solution

Figure B.15: Well index results using a 9-block unstructured approach for the DEL-GT-02-S2 well. The full solution (a) and a normalized error (b) using the Peaceman well index are shown.

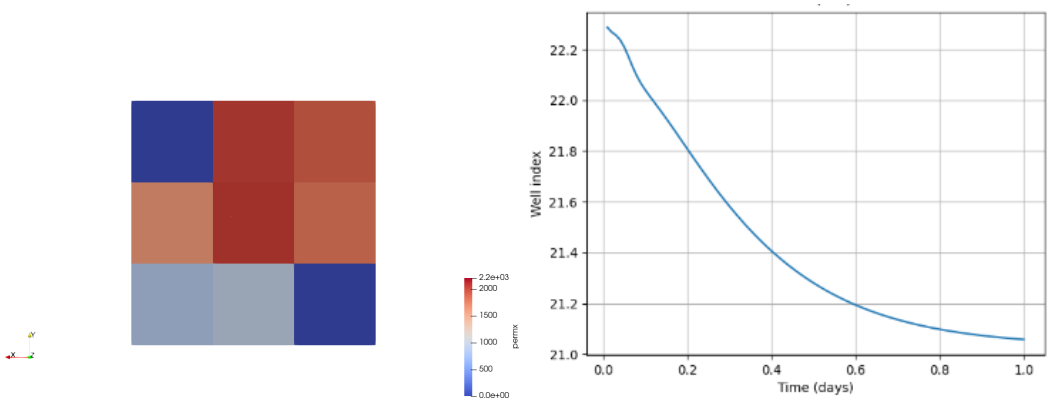

(a) Permeability profile **(b)** Simulation solution

Figure B.16: The permeability profile of reservoir block with index (61, 61, 6) for the DEL-GT-01 well in the 9-block case (a) and the obtained solution following simulation in DARTS with the defined timing parameters.

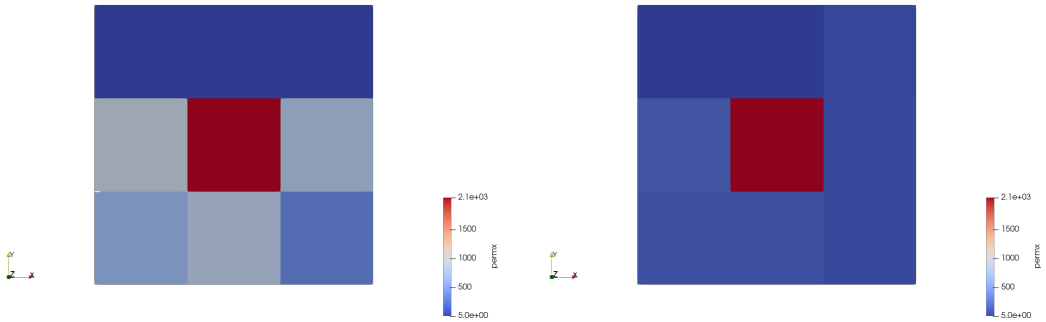

(a) (62, 61, 33) **(b)** (62, 61, 34)

Figure B.17: The permeability profiles of well blocks with indices (62, 61, 33) and (62, 61, 34).